

## MATERIALS SCIENCE

Strategies in catalysts and electrolyzer design for electrochemical CO<sub>2</sub> reduction toward C<sub>2+</sub> productsLei Fan<sup>1,2\*</sup>, Chuan Xia<sup>2,3\*</sup>, Fangqi Yang<sup>4</sup>, Jun Wang<sup>4</sup>, Haotian Wang<sup>2,5†</sup>, Yingying Lu<sup>1†</sup>

In light of environmental concerns and energy transition, electrochemical CO<sub>2</sub> reduction (ECR) to value-added multicarbon (C<sub>2+</sub>) fuels and chemicals, using renewable electricity, presents an elegant long-term solution to close the carbon cycle with added economic benefits as well. However, electrocatalytic C—C coupling in aqueous electrolytes is still an open challenge due to low selectivity, activity, and stability. Design of catalysts and reactors holds the key to addressing those challenges. We summarize recent progress in how to achieve efficient C—C coupling via ECR, with emphasis on strategies in electrocatalysts and electrocatalytic electrode/reactor design, and their corresponding mechanisms. In addition, current bottlenecks and future opportunities for C<sub>2+</sub> product generation is discussed. We aim to provide a detailed review of the state-of-the-art C—C coupling strategies to the community for further development and inspiration in both fundamental understanding and technological applications.

## INTRODUCTION

The excessive release of carbon dioxide (CO<sub>2</sub>) into atmosphere has triggered serious environmental consequences and also presents an urgent and potentially irreversible threat to human societies (1, 2). As the atmospheric CO<sub>2</sub> concentration increased sharply from 270 ppm (parts per million) in the early 1800s to 401.3 ppm in July 2015, a worldwide consensus on recycling the carbon footprint emitted by human activities has been reached (3, 4). To realize the close loop for carbon footprint, one potential approach is to shift the dependence of current energy and chemical industries away from fossil fuels into renewable sources such as solar and wind (5–8). However, the fraction of energy from those renewable sources is only limited to 30% owing to their intermittent nature, unless approaches for large-scale energy storage become available (9). Hence, as an alternative, capture of CO<sub>2</sub> from point sources such as power plants, followed by conversion into chemical feedstocks and fuels, is more practically viable (9–12). Electrocatalytic CO<sub>2</sub> reduction (ECR) using renewable electricity represents an elegant long-term solution due to the mild operation conditions required for the conversions, in which value-added products could be selectively produced (13). As schematically illustrated in Fig. 1, in this process, the electrochemical electrolyzer converts CO<sub>2</sub> and water into chemicals and fuels powered by renewable electricity. The resulting fuel is capable of long-term storage and can also be distributed or consumed, giving off CO<sub>2</sub> as the main waste, which will be captured and fed back to the reactor to close the loop. Moreover, the resulting small-molecule chemical feedstocks [e.g., carbon monoxide (CO) and formate] from ECR can be used as raw materials for more complicated chemical synthesis.

However, CO<sub>2</sub> is a quite stable linear molecule with a strong C=O bond (750 kJ mol<sup>−1</sup>) (14), making it difficult for electrochem-

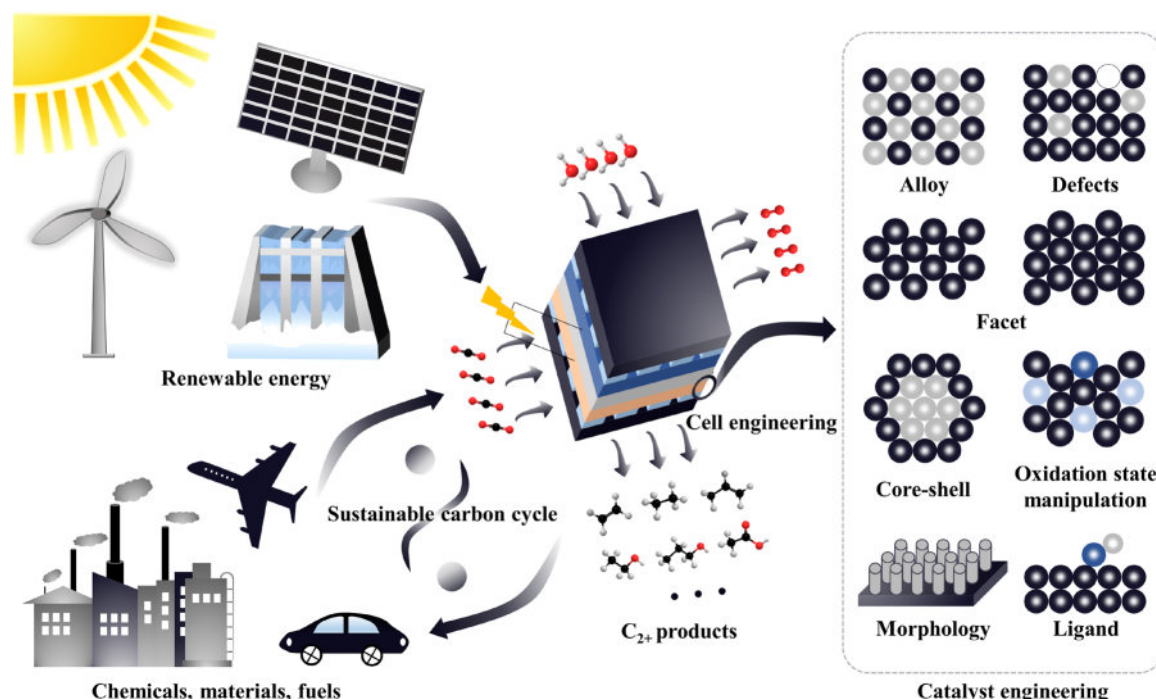
ical conversion. Thus, it requires a high activation barrier, which, in turn, leads to significant overpotentials (15). Furthermore, ECR in an aqueous electrolyte involves multi-electron/proton transfer processes together with a number of different possible reaction intermediates and products (16–18), making it highly complex. Table 1 summarizes the half electrochemical thermodynamic reactions of the main ECR products, including CO, methane (CH<sub>4</sub>), methanol (CH<sub>3</sub>OH), formic acid (HCOOH), ethylene (C<sub>2</sub>H<sub>4</sub>), ethanol (CH<sub>3</sub>CH<sub>2</sub>OH), and so on, together with their corresponding standard redox potentials (19). In general, during an ECR process, CO<sub>2</sub> molecules first undergo adsorption and interaction with atoms on the catalyst surface to form \*CO<sub>2</sub><sup>−</sup>, followed by various stepwise transfer of protons and/or electrons toward different final products. For example, CH<sub>4</sub> is believed to form through the following pathways: CO<sub>2</sub> → \*COOH → \*CO → \*CHO → \*CH<sub>2</sub>O → \*CH<sub>3</sub>O → CH<sub>4</sub> + \*O → CH<sub>4</sub> + \*OH → CH<sub>4</sub> + H<sub>2</sub>O (20).

Figure 2A summarizes the Faradaic efficiency (FE) under different production rates (current density) for the reported ECR electrocatalysts, which represents the product selectivity of the reaction (21–43). Notably, while the state-of-the-art electrocatalysts can transform CO<sub>2</sub> into C<sub>1</sub> products (CO or formate) with over 95% FE under high production rate (>20 mA cm<sup>−2</sup> for H-type cell and >100 mA cm<sup>−2</sup> for flow cell) (9, 21, 22, 25, 28, 44, 45), the highly selective (>90%) and efficient production of more available multicarbon (C<sub>2+</sub>) chemicals has not been realized so far. This is due to the fact that coupling to C<sub>2+</sub> products requires arrival and adsorption of several CO<sub>2</sub> molecules to the surface, stepwise transformation, and spatial positioning (13). To be specific, as shown in Fig. 2B, the subsequent reactions of \*CO intermediates determine the final C<sub>2+</sub> products of ECR. In general, C<sub>2</sub>H<sub>6</sub> and CH<sub>3</sub>COO<sup>−</sup> share the same \*CH<sub>2</sub> intermediate, which is generated from the proton-coupled electron transfer steps of \*CO. Further protonation of \*CH<sub>2</sub> gives \*CH<sub>3</sub> intermediate, which leads to the formation of C<sub>2</sub>H<sub>6</sub> via \*CH<sub>3</sub> dimerization. Unlike C<sub>2</sub>H<sub>6</sub> generation, CH<sub>3</sub>COO<sup>−</sup> is formed by CO insertion into \*CH<sub>2</sub>. The \*CO dimerization is the rate-determining step for C<sub>2</sub>H<sub>4</sub>, CH<sub>3</sub>CH<sub>2</sub>OH, and *n*-propanol (*n*-C<sub>3</sub>H<sub>7</sub>OH) formation. After a series of electron transfer and protonation steps, the \*CO—CO dimer forms the \*CH<sub>2</sub>CHO intermediate, which serves as the selectivity-determining step for C<sub>2</sub>H<sub>4</sub> and C<sub>2</sub>H<sub>5</sub>OH. In addition, it was found that reducing \*CH<sub>2</sub>CHO to C<sub>2</sub>H<sub>4</sub> has lower energy barrier than transforming \*CH<sub>3</sub>CHO to

<sup>1</sup>State Key Laboratory of Chemical Engineering, Institute of Pharmaceutical Engineering, College of Chemical and Biological Engineering, Zhejiang University, Hangzhou 310027, China. <sup>2</sup>Department of Chemical and Biomolecular Engineering, Rice University, Houston, TX 77005, USA. <sup>3</sup>Smalley-Curl Institute, Rice University, Houston, TX 77005, USA. <sup>4</sup>School of Resource, Environmental and Chemical Engineering, Nanchang University, Nanchang 330031, Jiangxi, China. <sup>5</sup>Azrieli Global Scholar, Canadian Institute for Advanced Research (CIFAR), Toronto, 22 Ontario M5G 1M1, Canada.

\*These authors contributed equally to this work.

†Corresponding author. Email: yingyinglu@zju.edu.cn (Y.L.); htwang@rice.edu (H.W.)



**Fig. 1. Schematic illustration of sustainable energy cycling based on ECR.** Fuels and chemicals could be achieved from ECR with closed carbon cycle powered by renewable energy sources such as solar, wind, and hydro. Cell engineering and catalyst engineering play key roles to promote the selectivity, activity, and efficiency for CO<sub>2</sub> conversion into value-added C<sub>2+</sub> products with high energy density.

C<sub>2</sub>H<sub>5</sub>OH (46), which may explain the higher FE for C<sub>2</sub>H<sub>4</sub> over C<sub>2</sub>H<sub>5</sub>OH on most copper catalysts. Furthermore, stabilized C<sub>2</sub> intermediates could transfer to *n*-C<sub>3</sub>H<sub>7</sub>OH via CO insertion. The complex and uncontrollable reaction pathways during C<sub>2+</sub> chemical formation are mainly due to many more permutations to the protonation sites, along with the possible involvement of nonelectrochemical step (19, 47). As such, the design of highly selective electrocatalysts is a prerequisite for specific C<sub>2+</sub> product formation at high yield. In this review, we aim to highlight the recent progress on strategies in electrocatalyst design for selective C<sub>2+</sub> product generation via ECR. We also provide a summary of the understandings of related mechanisms. Electrode and reactor design will also be emphasized to show how to achieve efficient, stable, and large-scale operation of ECR. Furthermore, we will discuss the remaining challenges and future opportunities for electrochemical conversion of CO<sub>2</sub> into value-added C<sub>2+</sub> chemicals.

Electrocatalytic transformation of CO<sub>2</sub> into chemical fuels and feedstocks is a potential technology to achieve a carbon-neutral energy cycle (11). However, the FE of C<sub>2+</sub> products is still far from practical application, where state-of-the-art catalysts allow production of C<sub>2</sub> products with around 60% FE (13, 33), while the C<sub>3</sub> production is limited to less than 10% FE (48, 49). Reductive coupling of CO<sub>2</sub> to C<sub>2+</sub> products requires heterogeneous catalysts with highly coordinated morphological and electronic properties (50, 51). The catalytic surface needs to break the scaling relations between the intermediates (47, 52, 53). Moreover, to achieve C—C bond formation, the adsorbed reaction intermediates at the catalyst surface must be in close proximity to one another. Furthermore, the pathway from the initially adsorbed intermediate toward a specific C<sub>2+</sub> product needs to be well controlled because of the multiple proton-assisted electron transfer steps. Con-

sidering the high complexity of CO<sub>2</sub> reduction toward C<sub>2+</sub> products, electrocatalysts should be carefully tailored to increase the selectivity. According to the intermediate species and chemical compositions, we categorize C<sub>2+</sub> products into multicarbon hydrocarbons and oxygenates (4, 54). To approach highly efficient electrocatalysts for specific C<sub>2+</sub> molecule production, several catalyst design strategies, such as heteroatom doping, crystal facet regulation, alloy/dealloying, oxidation state tuning, and surface ligand control, have been demonstrated (35, 41, 55–61). Optimal design should rationally consider the aforementioned effects and maximize the benefits. Otherwise, understanding what active-site motifs lead to such a unique catalytic behavior may further shine a light on precise catalyst design for C—C coupling. Hence, how to design ECR catalyst toward specific products (multicarbon hydrocarbons and oxygenates) and the related mechanism will be discussed in this part.

### MULTICARBON HYDROCARBONS

C<sub>2+</sub> hydrocarbons, such as C<sub>2</sub>H<sub>4</sub>, are nexus chemicals for a variety of chemical industries, such as polyethylene production (62, 63). Besides, it could be directly used as the fuel for welding or a mixed component in natural gas (12). Hydrogenation of CO (Fischer-Tropsch synthesis) and CO<sub>2</sub> has been used to produce C<sub>2+</sub> hydrocarbons for a long time in industrial scale but challenged by high energy consumption and environmental impact (64). In stark contrast, electrochemical CO<sub>2</sub> reduction using renewable energy provides a cleaner and more sustainable route. Great effort has been made to develop efficient electrocatalysts toward C<sub>2+</sub> hydrocarbons (32, 33, 65–70).

Bimetallic electrocatalysts have been widely investigated to break the scaling relationship during electrochemical CO<sub>2</sub> conversion, which

**Table 1. Half electrochemical thermodynamic reactions of the main ECR production, together with their corresponding standard redox potentials [V versus reversible hydrogen electrode (RHE)].**

Products	Acid		Base	
	Equation	<i>E</i> (V)	Equation	<i>E</i> (V)
Hydrogen	$2\text{H}^+ + 2\text{e}^- \rightarrow \text{H}_2$	0.000	$2\text{H}_2\text{O} + 2\text{e}^- \rightarrow \text{H}_2 + 2\text{OH}^-$	−0.828
Carbon monoxide	$\text{CO}_2 + 2\text{H}^+ + 2\text{e}^- \rightarrow \text{CO} + \text{H}_2\text{O}$	−0.104	$\text{CO}_2 + \text{H}_2\text{O} + 2\text{e}^- \rightarrow \text{CO} + 2\text{OH}^-$	−0.932
Methane	$\text{CO}_2 + 8\text{H}^+ + 8\text{e}^- \rightarrow \text{CH}_4 + 2\text{H}_2\text{O}$	0.169	$\text{CO}_2 + 6\text{H}_2\text{O} + 8\text{e}^- \rightarrow \text{CH}_4 + 8\text{OH}^-$	−0.659
Methanol	$\text{CO}_2 + 6\text{H}^+ + 6\text{e}^- \rightarrow \text{CH}_3\text{OH} + \text{H}_2\text{O}$	0.016	$\text{CO}_2 + 5\text{H}_2\text{O} + 6\text{e}^- \rightarrow \text{CH}_3\text{OH} + 6\text{OH}^-$	−0.812
Formic acid/formate	$\text{CO}_2 + 2\text{H}^+ + 2\text{e}^- \rightarrow \text{HCOOH}$	−0.171	$\text{CO}_2 + \text{H}_2\text{O} + 2\text{e}^- \rightarrow \text{HCOO}^- + \text{OH}^-$	−0.639
Ethylene	$2\text{CO}_2 + 12\text{H}^+ + 12\text{e}^- \rightarrow \text{C}_2\text{H}_4 + 4\text{H}_2\text{O}$	0.085	$2\text{CO}_2 + 8\text{H}_2\text{O} + 12\text{e}^- \rightarrow \text{C}_2\text{H}_4 + 12\text{OH}^-$	−0.743
Ethane	$2\text{CO}_2 + 14\text{H}^+ + 14\text{e}^- \rightarrow \text{C}_2\text{H}_6 + 4\text{H}_2\text{O}$	0.144	$2\text{CO}_2 + 10\text{H}_2\text{O} + 14\text{e}^- \rightarrow \text{C}_2\text{H}_6 + 14\text{OH}^-$	−0.685
Ethanol	$2\text{CO}_2 + 12\text{H}^+ + 12\text{e}^- \rightarrow \text{CH}_3\text{CH}_2\text{OH} + 3\text{H}_2\text{O}$	0.084	$2\text{CO}_2 + 9\text{H}_2\text{O} + 12\text{e}^- \rightarrow \text{CH}_3\text{CH}_2\text{OH} + 12\text{OH}^-$	−0.744
Acetic acid/acetate	$2\text{CO}_2 + 8\text{H}^+ + 8\text{e}^- \rightarrow \text{CH}_3\text{COOH} + 2\text{H}_2\text{O}$	0.098	$2\text{CO}_2 + 5\text{H}_2\text{O} + 8\text{e}^- \rightarrow \text{CH}_3\text{COO}^- + 7\text{OH}^-$	−0.653
<i>n</i> -Propanol	$3\text{CO}_2 + 18\text{H}^+ + 18\text{e}^- \rightarrow \text{CH}_3\text{CH}_2\text{CH}_2\text{OH} + 5\text{H}_2\text{O}$	0.095	$3\text{CO}_2 + 13\text{H}_2\text{O} + 18\text{e}^- \rightarrow \text{CH}_3\text{CH}_2\text{CH}_2\text{OH} + 18\text{OH}^-$	−0.733

can stabilize the key intermediate and lower the overpotential and, thus, in turn, increase the selectivity (71–74). While a series of alloy materials including Au–Cu, Ag–Cu, Au–Pd, and Cu–Pt have been demonstrated for high efficiency  $\text{C}_1$  production by stabilizing the critical intermediate (73, 75), the alloy effect toward  $\text{C}_{2+}$  hydrocarbon formation seems to be more complex (76). For example, in the Cu–Ag bimetallic system, the product distribution can be easily controlled by tuning the surface atomic ratio of Ag and Cu (77). The surface Cu-rich sample is preferred for hydrocarbon production, while the products of the surface Ag-rich one are dominated by CO, highlighting the importance of atomic ratio for alloyed ECR electrocatalysts. The geometric effect caused by the local atomic arrangement can significantly affect the binding strength of the intermediates. Gewirth and co-workers (36) showed that Cu–Ag alloys from additive-controlled electrodeposition exhibited ~60% FE for  $\text{C}_2\text{H}_4$  in an alkaline flow electrolyzer (Fig. 3, A and B). In this case, optimized  $\text{C}_2\text{H}_4$  selectivity can be achieved by morphology and Ag-loading tuning. The Ag sites were believed to play the role of a promoter for CO formation during ECR. Then, the optimal availability of the CO intermediate could help the C–C coupling in the neighboring Cu. Besides, Ag can also promote the formation of  $\text{Cu}_2\text{O}$  during the Cu–Ag catalyst synthesis (Fig. 3C), resulting in enhanced  $\text{C}_2\text{H}_4$  production efficiency. This synergy opens up new possibilities for developing C–C coupling catalysts. Furthermore, the mixing pattern of different metals in the alloy system could also determine the distribution of ECR products. Using Pd–Cu alloy as an example (Fig. 3D), Kenis and co-workers (71) demonstrated that a phase-separated Pd–Cu catalyst can offer the highest selectivity (~50%) for  $\text{C}_2\text{H}_4$  compared with its ordered and disordered counterparts. According to the d-band theory, typically, transition metal with a lower d-band center shows weaker binding of the in situ generated intermediates on the metal surfaces (78). While phase-separated

Pd–Cu alloy exhibited similar catalytic selectivity and activity for CO with Cu nanoparticles (NPs), it offered completely different binding strength toward intermediates by Pd tuning. As shown in Fig. 3E, phase-separated Cu–Pd alloy showed the lowest-lying d-band center, whereas that of Cu NP is the highest. It suggests that the phase-separated Cu–Pd alloy had the lowest binding strength for the CO intermediate. This observation implies that the geometric and structure effect may play a greater role than the electronic effect for improving the hydrocarbon selectivity in the phase-separated Cu–Pd alloy case. To date, only pure copper or copper-based alloy shows superior selectivity and activity for electrochemical reduction of  $\text{CO}_2$  to  $\text{C}_{2+}$  hydrocarbons. Thus, it is very necessary to develop a novel electrocatalyst for  $\text{C}_{2+}$  hydrocarbon production from ECR. Inspired by  $\text{CO}_2$  hydrogenation, a preliminary study demonstrated that Ni–Ga alloy with different phases could be used for  $\text{C}_2\text{H}_4$  generation (79). It showed that  $\text{Ni}_5\text{Ga}_3$  film could reduce  $\text{CO}_2$  to  $\text{C}_2\text{H}_4$  and ethane ( $\text{C}_2\text{H}_6$ ). Although the FE toward  $\text{C}_{2+}$  hydrocarbons is less than 5%, it may open new lines for electrocatalyst screening toward C–C coupling based on the alloy effect.

Besides alloy effect, manipulating the oxidation states is another major principle to tune the performance of electrocatalysts, which can affect the local electronic structure of the material. The first example for the oxidation state tuning of catalyst is to use oxide-derived materials. The residual oxygen species on the surface or subsurface of catalyst after in situ reduction can regulate the oxidation state of the metal center. For example, plasma-oxidized Cu showed more than 60% selectivity toward  $\text{C}_2\text{H}_4$ , which was ascribed to the reduction-resistant  $\text{Cu}^+$  (37). To confirm that  $\text{Cu}^+$  is the key parameter for high ethylene selectivity, we performed control experiments using different plasma (Fig. 4A). In situ hard x-ray absorption spectroscopy further showed that the residual oxides in the (sub)surface layer are stable against reduction condition, with a significant amount of  $\text{Cu}^+$  species

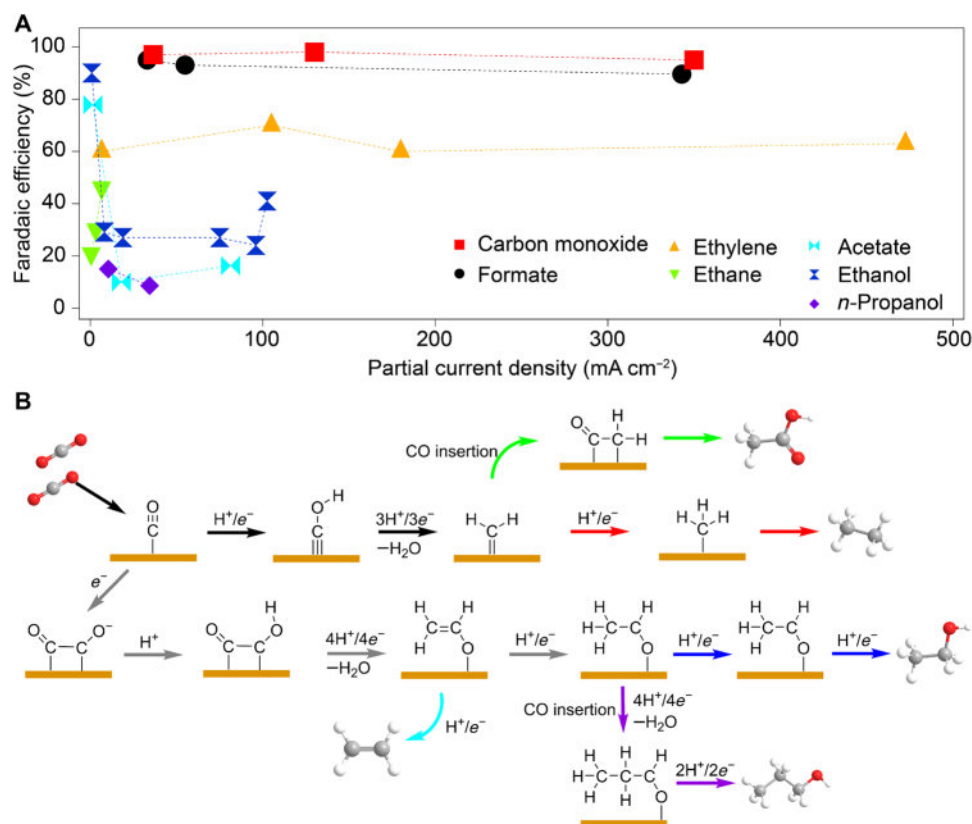


**Fig. 2. Summary of the state-of-the-art ECR performance and the C–C coupling mechanisms.** (A) The FE under different production rates (current density) for the reported ECR electrocatalysts (21–43, 130). (B) Most possible C<sub>2+</sub> pathways during ECR. Reproduced with permission from the American Chemical Society (47).

remaining after 1 hour of reduction at relatively high potentials of  $-1.2$  V versus reversible hydrogen electrode (RHE). Furthermore, electroreduction of copper from a sol-gel copper oxychloride verified again that stabilized surface Cu<sup>+</sup> species could improve the selectivity of C<sub>2</sub>H<sub>4</sub> (61). The oxidation state of a copper catalyst under different applied potentials was tracked using time-resolved in situ soft x-ray absorption spectroscopy. The initial transition step from Cu<sup>2+</sup> to Cu<sup>+</sup> is very quick; however, the further electrochemical reduction of Cu<sup>+</sup> species to Cu<sup>0</sup> is much slower. Around 23% of Cu<sup>+</sup> species remain even after 1-hour constant reduction under  $-1.2$  V versus RHE (Fig. 4B). Mechanistic studies revealed that the interface between Cu<sup>+</sup> and Cu<sup>0</sup> leads to electrostatic attraction between intermediates since the C atom of \*CO@Cu<sup>+</sup> is positively charged, whereas that of \*CO@Cu<sup>0</sup> is negatively charged (80), which, in turn, promotes the C–C bond formation and thus produces C<sub>2+</sub> hydrocarbons. In addition to oxide-derived materials, copper nitride (Cu<sub>3</sub>N) was also used to achieve (sub)surface Cu<sup>+</sup> species to decrease the dimerization energy barrier of \*CO (81). In addition, compared with oxide-derived Cu, Cu<sub>3</sub>N-derived Cu<sup>+</sup> species are even more stable (Fig. 4C). As a result, the nitride-derived copper catalyst exhibits an FE of  $39 \pm 2\%$  for C<sub>2</sub>H<sub>4</sub>, outperforming the pure Cu ( $\sim 23\%$ ) and oxide-derived Cu ( $\sim 28\%$ ). Analogous to the abovementioned Cu<sup>+</sup>/Cu catalytic system, boron has been used as a heteroatom dopant to introduce and stabilize Cu<sup>δ+</sup> (41). The average oxidation state of copper can be controlled from  $+0.25$  to  $+0.78$  by changing the concentration of boron dopant. Projected density of states showed that the electrons transferred from copper to boron, leading to a dopant-induced positively charged copper

sites. The boron-doped copper showed an increased formation energy of \*CHO intermediate and, thus, suppressed the reaction pathway toward C<sub>1</sub> products. In addition, it can increase the selectivity toward multicarbon hydrocarbons by decreasing \*CO dimerization reaction energy (Fig. 4D). By optimizing the average surface oxidation state of copper, a high C<sub>2</sub> FE of  $\sim 80\%$  with  $\sim 53\%$  C<sub>2</sub>H<sub>4</sub> could be achieved under an average copper oxidation state of  $+0.35$  (Fig. 4E). To date, the active sites on copper have been identified as Cu<sup>0</sup>, Cu<sup>δ+</sup>, and/or their interface for ECR in different studies (39, 41, 42, 81, 82). However, what is the active site is still being debated. While the heteroatom doping-induced Cu<sup>δ+</sup> catalysts have been demonstrated to be very active for ECR toward C<sub>2+</sub> products, the synergistic effect from the simultaneously generated defects and interfaces should also be considered. Hence, systematic in operando characterizations should be developed to identify the active center on copper surface and monitor the potential in situ transformation of the active sites under reaction conditions. Besides, the stability of the positively charged copper is another concern under electrochemical reduction conditions. How to synthesize catalysts with stable Cu<sup>δ+</sup> sites remains a challenge.

Apart from the electronic structure, oxide-derived materials can also lead to morphology or structure evolution during the in situ reduction process. From the perspective of morphology or structure, the enhanced electrochemical performance of oxide-derived electrocatalysts has been attributed to the formation of active grain boundaries, edges, and steps (83–85). Yeo and co-workers (83) reported the selective C–C coupling on electrodeposited Cu<sub>2</sub>O films with different thicknesses (Fig. 4F). In situ Raman spectroscopy revealed that the surface of



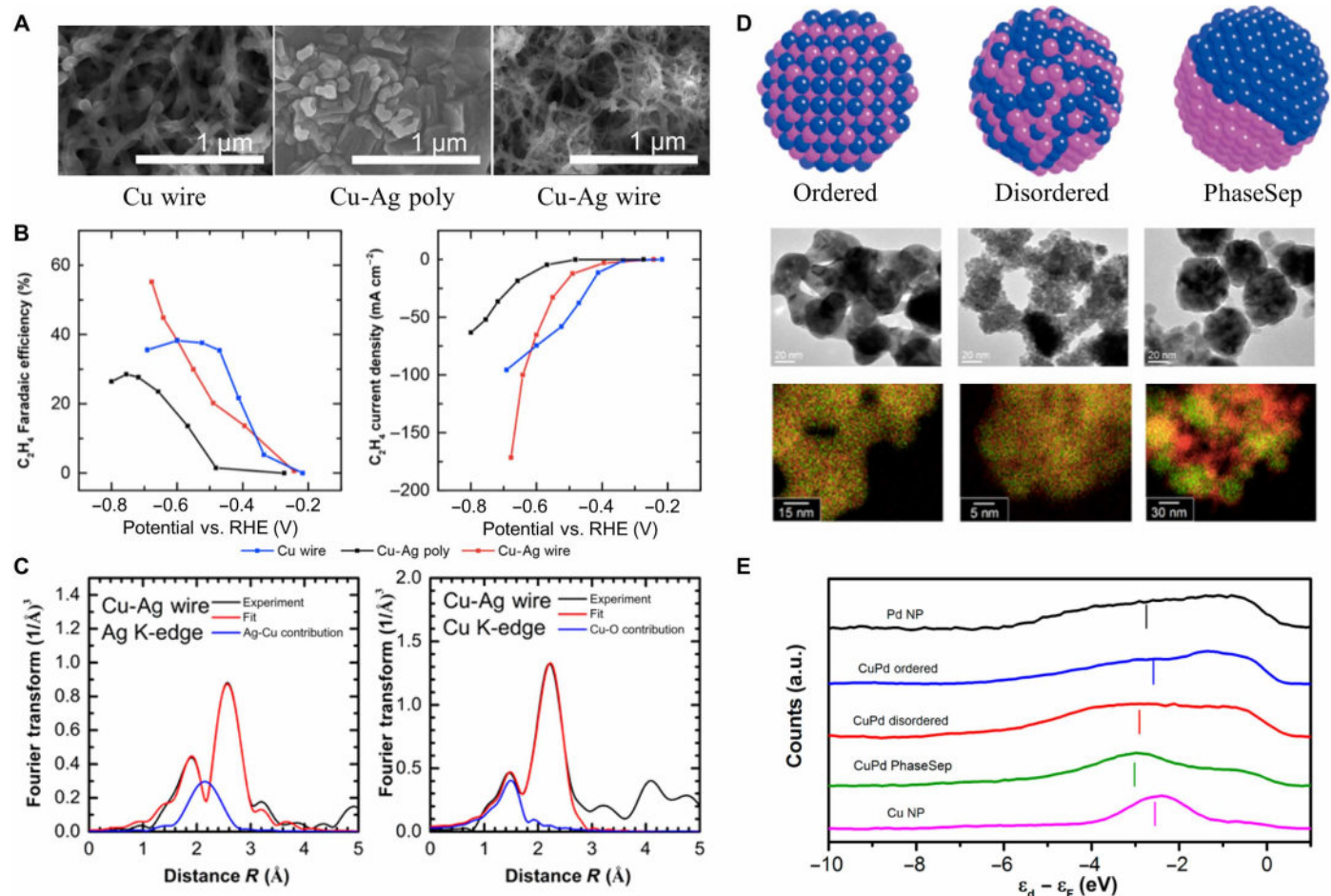


**Fig. 3. Alloy effects of ECR catalyst toward  $C_2+$  hydrocarbons.** (A to C) Cu-Ag bimetallic catalysts fabricated by additive-controlled electrodeposition: (A) scanning electron microscopy (SEM) of Cu wire, Cu-Ag poly, and Cu-Ag wire and (B) corresponding  $C_2H_4$  FE. (C) EXAFS showed that Cu-Ag wire was homogeneously mixed and Cu(I) oxide was presented. (A) to (C) are reproduced with permission from the American Chemical Society (36). (D and E) Cu-Pd catalysts with different mixing patterns: (D) Illustration, transmission electron microscopy (TEM) images, and energy-dispersive spectroscopy element maps of ordered, disordered, and phase-separated Cu-Pd alloys and (E) surface valence band photoemission spectra and d-band center (the vertical line) of Cu-Pd alloys relative to Fermi level. (D) and (E) are reproduced with permission from the American Chemical Society (71). a.u., arbitrary units.

the  $Cu_2O$  films was reduced to stable metallic  $Cu^0$  during ECR (83). As a result, metallic  $Cu^0$  has been confirmed as the catalytic active center instead of  $Cu^+$  species or the  $Cu^+/Cu^0$  interface. In the process of reducing  $Cu_2O$  to metallic  $Cu^0$ , the catalyst surface is likely to in situ form steps, edges, and terraces. It was pointed out that the formed steps and edges are more active than the terraces, originating from their stronger binding with  $*CO$ , which can further hydrogenate  $*CO$  to  $*CHO$  or  $*CH_2O$ . Besides, edge Cu atoms are a promoter to boost  $*CHO$  and  $*CH_2O$  formation. Previous work suggested that  $*CHO$  and  $*CH_2O$  intermediates are more favorable for C–C coupling than  $*CO$  in kinetics (86). By regulating the surface morphology, the chemisorption energies of the  $*CHO$  and  $*CH_2O$  intermediates can be optimized. In this study, the authors found that the FE of  $C_2H_4$  decreased from 40 to 22% when they increased the thickness of  $Cu_2O$  thin film from 0.9 to 8.8  $\mu m$ . This is due to the concentration of low coordinated Cu that increased with the increase in  $Cu_2O$  thickness. These undercoordinated atoms can strongly bind with H and, thus, are more preferred for hydrogen evolution than C–C coupling. This work demonstrated that the oxide-derived copper catalyst can sig-

nificantly enhance the  $C_2H_4$  selectivity via surface morphology reconstruction instead of introducing charged  $Cu^{\delta+}$  species. Using the oxide-derived catalysts, ethane ( $C_2H_6$ ) has also been selectively produced with the help of palladium(II) chloride ( $PdCl_2$ ) additive in electrolyte (34). It showed that the adsorbed  $PdCl_x$  on the surface of  $Cu_2O$ -derived Cu played a vital role for  $C_2H_6$  evolution. Specifically,  $CO_2$  was firstly reduced to  $C_2H_4$  at the  $Cu_2O$ -derived active Cu sites, and then the formed  $C_2H_4$  would be hydrogenated with the assistance of adsorbed  $PdCl_x$  to produce  $C_2H_6$ . The FE of  $C_2H_6$  increased from <1 to 30.1% with the assistance of  $PdCl_2$ . This work suggests that the combination of the well-defined ECR catalyst and electrolyte additive may open up new opportunities for specific  $C_2+$  product generation.

Morphology and/or structure regulation represents another alternative strategy to modulate catalytic selectivity and activity. Controlling the size, shape, and exposed facets of catalyst has been widely demonstrated for ECR performance improvement (58, 87, 88). For example, the Cu(100) facet is intrinsically preferred for  $C_2H_4$  generation, while the dominated product from the Cu(111) catalyst is methane ( $CH_4$ ) (87). In a study of Cu nanocrystals with various shapes and

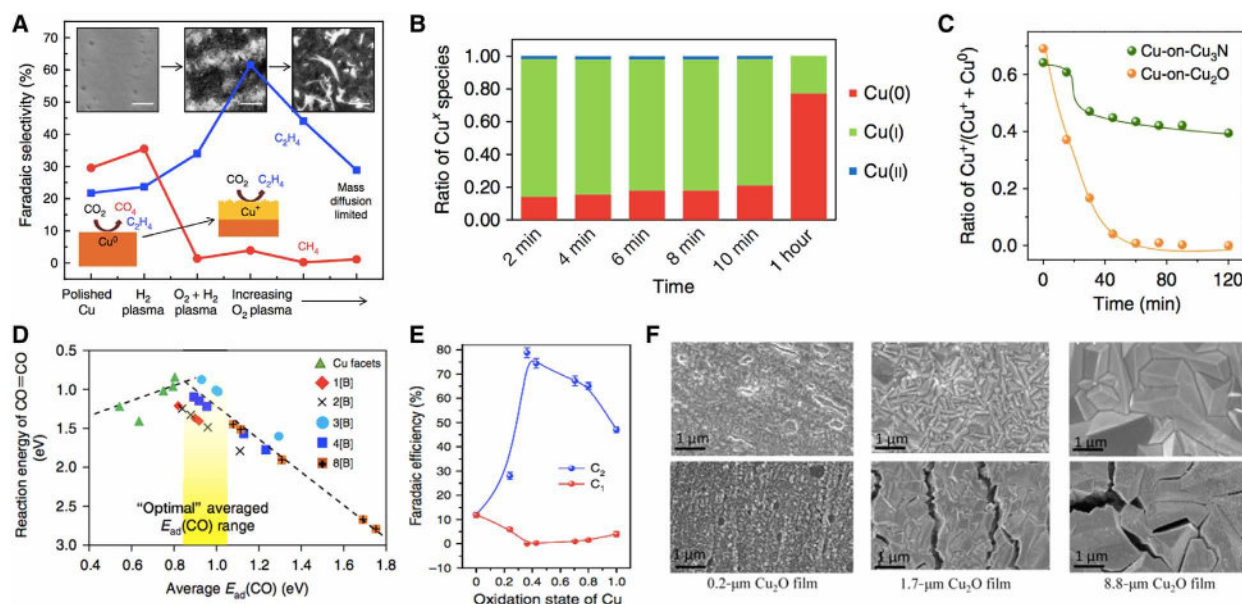


**Fig. 4. Oxidation states changing induced effects for  $C_2+$  hydrocarbon production.** (A) Summary of the  $C_2H_4$  selectivity of different plasma-activated copper catalysts. Reproduced with permission from the Nature Publishing Group (37). Scale bars, 500 nm. (B) Ratio of Cu oxidation states relative to the reaction time at  $-1.2$  V versus RHE in electrodeposited copper. Reproduced with permission from the Nature Publishing Group (61). (C) Ratio of  $Cu^+$  species with a function of reaction time at  $-0.95$  V versus RHE in  $Cu-on-Cu_3N$  or  $Cu-on-Cu_2O$ . Reproduced with permission from the Nature Publishing Group (81). (D) Boron doping was able to change the average adsorption energy of CO in the copper surface and lower the CO—CO dimerization energy. 1[B], 2[B], 3[B], 4[B], and 8[B] refer to the concentration of subsurface boron doping in the copper catalysts, which were 1/16, 1/8, 3/16, 1/4, and 1/2, respectively. (E) The relationship between the oxidation state and FE of  $C_2$  or  $C_1$  products in boron-doped copper catalysts. (D) and (E) are reproduced with permission from the Nature Publishing Group (41). (F) SEM images of copper foils with different thicknesses of  $Cu_2O$  films before (top) and after (bottom) ECR. Reproduced with permission from the American Chemical Society (83).

sizes, Buonsanti and co-workers (58) revealed a nonmonotonic size dependence of the  $C_2H_4$  selectivity in cube-shaped copper nanocrystals (Fig. 5A). Intrinsically, cubic Cu nanocrystals exhibited higher  $C_2H_4$  activity and selectivity than spherical Cu nanocrystals owing to the predominance of the (100) facet. The smaller crystal size of cubic Cu could offer higher activity because of the increased concentration of low-coordinated surface sites, such as corners, steps, and kinks. However, the stronger chemisorption of low-coordinated sites was accompanied by higher  $H_2$  and CO selectivity, resulting in lower overall hydrocarbon FE. On the other hand, the ratio of edge sites to plane sites decreased with the increase in particle sizes, which also affects the performance of  $C_2H_4$  production. The authors demonstrated that intermediate-sized copper nanocubes with a 44-nm edge length displayed the highest  $C_2H_4$  selectivity due to the optimized balance between particle size and the density of edge sites. Furthermore, morphology can also affect the local pH and mass transport during ECR. It has been demonstrated that the high local pH in the vicinity of catalyst surface, which is caused by the in situ generated  $OH^-$ , suppresses the proton-involved reaction pathway. As a result,  $C_2+$  hydrocarbon formation through  $*CO$  dimerization could be enhanced, and  $CH_4$  formed through  $*COH$  intermediate might be inhibited. Copper nanowire arrays (Fig. 5B) have been demonstrated to achieve increased local pH (68). As a commonly used electrolyte,  $CO_2$  saturated potassium bicarbonate ( $KHCO_3$ ) solution will quickly neutralize the local  $OH^-$  ( $HCO_3^- + OH^- = CO_3^{2-} + H_2O$ ) and decrease the local pH. With an elongated microstructure, the diffusion of  $HCO_3^-$  into the Cu nanowire arrays can be somehow undermined so that the neutralization effect for local  $OH^-$  will be suppressed to some degree. On the basis of a similar principle, copper meshes with precisely controlled mesopores

(Fig. 5C) demonstrated enhanced FE for  $C_2H_4$  or  $C_2H_6$  production (32). It showed that the local pH in the electrode surface could be increased by narrowing the pore width, resulting in decreased  $C_1$  product FE and enhanced  $C_2$  product FE. Besides, by increasing the pore depth, the major reduction product could be tuned from  $C_2H_4$  to  $C_2H_6$ . The FE of  $C_2H_6$  was as high as 46%. Since the chemicals have been confined inside the pores during ECR, prolonged retention time of the key intermediates caused by the deeper pores has been explained as the main reason for the high selectivity toward saturated  $C_2$  hydrocarbon. CuI-derived Cu nanofibers also showed high selectivity toward  $C_2H_6$  (FE = 30% at  $-0.735$  V versus RHE) (89). The anisotropic morphology and high surface roughness of CuI-derived Cu nanofibers can improve the trapping efficiency of absorbed  $H_2$  and thus increase the FE of  $C_2H_6$ .

Catalyst surface modification using small molecules is another well-known strategy to improve the electrochemical performance of ECR. This strategy can influence the microenvironment near the catalyst surface, which may stabilize the key intermediates due to the interaction between surface ligand and intermediate. Amine has been reported as a modifier to promote ECR (35). Various amino acids, including glycine (Gly), DL-alanine (Ala), DL-leucine (Leu), DL-tryptophan (Tyr), DL-arginine (Arg), and DL-tryptophan (Trp), have been investigated to study their effects on copper nanowires (35). As shown in Fig. 5D, all amino acid-based ligands were capable of improving the selectivity of  $C_2+$  hydrocarbons. Such an enhancement suggests that  $-COOH$  and  $-NH_2$  functional groups in amino acid are probably responsible for the enhanced selectivity of ECR. Previous reports illustrated that the adsorption of amino acids on the Cu surface was achieved through both  $-COOH$  and  $-NH_2$  groups (35, 90). Stearic

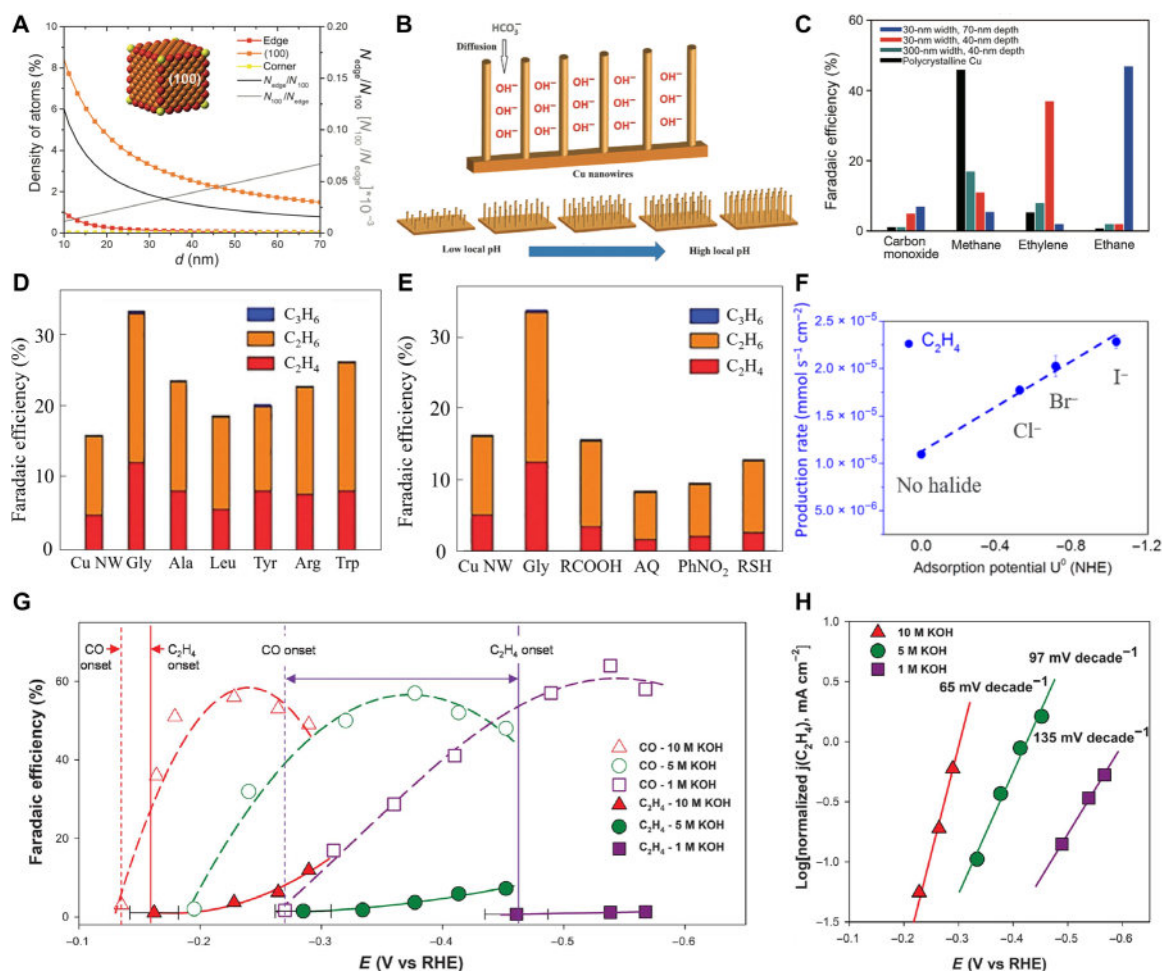


**Fig. 5. Morphology or structure and ligand effects for ECR toward  $C_{2+}$  hydrocarbons.** (A to C) Morphology or structure effects. (A) Density of atoms (left axis) and the ratio of atoms at the edge sites ( $N_{\text{edge}}$ ) to atoms on the (100) plane ( $N_{100}$ ) (right axis) in relevance to the edge length ( $d$ ). Reproduced with permission from John Wiley and Sons (58). (B) Scheme of morphology caused pH changing. Reproduced with permission from John Wiley and Sons (68). (C) Product selectivity of mesopore copper with different pore sizes and depths. Reproduced with permission from John Wiley and Sons (32). (D to H) Ligand effects. (D and E) ECR on copper nanowire (Cu NW) with different kinds of amino acids (D) or modifiers (E) at  $-1.9$  V. Reproduced with permission from the Royal Society of Chemistry (35). (F) Production rates of  $C_2H_4$  in different halide electrolytes with different adsorption potentials on Cu(35). Reproduced with permission from the American Chemical Society (91). NHE, normal hydrogen electrode. (G) FE of  $C_2H_4$  and CO in different concentrations of KOH electrolytes and (H) Tafel slope of  $C_2H_4$  in different concentrations of KOH electrolytes. (G) and (H) are reproduced from the American Association for the Advancement of Science (AAAS) (33).

acid ( $C_{17}H_{35}COOH$ ,  $RCO_2H$ ), which contains only the  $-COOH$  group, was selected to identify the role of  $-COOH$ . Other modifiers, such as *a*-anthraquinone diazonium salt (AQ), *o*-nitrobenzene diazonium salt ( $PhNO_2$ ), and dodecyl mercaptan ( $C_{12}H_{25}SH$ , RSH), which contain neither  $-COOH$  nor  $-NH_2$  groups, were also investigated. However, all of them were not positive for  $C_{2+}$  hydrocarbon FE improvement (Fig. 5E). Theoretical calculations indicated that  $-NH_3^+$  groups in the adsorbed zwitterionic glycine could stabilize  $*CHO$  intermediate due to their strong interaction, such as hydrogen bonds. Introduction of halide ions into the electrolyte is another way to modify the catalysts (91, 92). As shown in Fig. 5F,  $C_2H_4$  production rate on plasma-activated Cu could be significantly increased with the assistance of halide additives. It was shown that  $I^-$  ion is more active than  $Br^-$  and  $Cl^-$ , in agreement with the corresponding adsorption energy of  $I^-$ ,  $Br^-$ , and  $Cl^-$  on the Cu(100) facet (91). Besides halides, hydroxide ion also showed a positive effect on  $C_2H_4$  selectivity. Recently,

Sargent and co-workers (33) reported the  $CO_2$ -to- $C_2H_4$  conversion with  $\sim 70\%$  FE using concentrated potassium hydroxide (KOH) electrolyte (up to 10 M) in a flow cell. As shown in Fig. 5G, the onset potential of CO and  $C_2H_4$  in 10 M KOH electrolyte was much lower compared to that in 1 M KOH. Furthermore, the Tafel slopes (Fig. 5H) of  $C_2H_4$  formation decreased with the increase of hydroxide concentration ( $135$  mV decade $^{-1}$  in 1 M KOH and  $65$  mV decade $^{-1}$  in 10 M KOH), suggesting the transmutation of the overall rate-determining step. Density functional theory (DFT) results proved that the presence of concentrated hydroxides could lower the binding energy of the CO intermediate and also increased the charge imbalance between two carbon atoms in adsorbed OCCO intermediates. As a result, the OCCO intermediate would be further stabilized through a stronger dipole attraction, leading to lower activation energy barrier for CO dimerization, which will then improve the overall performance.



## MULTICARBON OXYGENATES

$C_{2+}$  oxygenates such as ethanol ( $CH_3CH_2OH$ ) are another major category of highly valuable ECR products. Industrial synthesis of ethanol is an energy-intensive process, which also consumes a large amount of ethylene or agricultural feedstocks (40). Thus, electrocatalytic production of ethanol or other  $C_{2+}$  oxygenates from  $CO_2$  makes a lot of economic and environmental sense. Since ethanol generation from ECR shared a penultimate intermediate with  $C_2H_4$  that is  $*C_2H_3O$  (43), selective hydrogenation of this intermediate could switch ECR pathways from  $C_2H_4$  to alcohols (64). However, in most systems, the selectivity toward  $C_{2+}$  oxygenates is much lower than hydrocarbons (31, 37, 39, 41, 42, 67). Thus, in this section, we will highlight the electrocatalyst design strategies that can achieve impressive  $C_{2+}$  oxygenate FE of over 25%.

As discussed above, well-designed bimetallic catalysts can improve the selectivity and activity for  $C_{2+}$  hydrocarbon production. A similar but not identical strategy has also been used to improve the electrocatalytic performance for  $C_{2+}$  oxygenates (38, 93, 94). For instance, Ag-incorporated Cu-Cu<sub>2</sub>O catalysts exhibited tunable ethanol selectivity, and the highest ethanol FE was 34.15% (95). The biphasic boundary in the phase-blended Ag-Cu alloy, instead of Ag/Cu atomic ratio, was identified as the key factor for selective production of ethanol. Since the Cu site is very close to the Ag site in a phase-blended pattern (Ag-Cu<sub>2</sub>O<sub>PB</sub>), the formation rate of ethanol intermediates for the phase-blended sample could be promoted in comparison to the phase-separated one (Ag-Cu<sub>2</sub>O<sub>PS</sub>), leading to a better ethanol generation performance. Besides ethanol, Cu-Ag bimetallic NPs have also been demonstrated to convert  $CO_2$  to acetate with the addition of benzotriazole (93). At  $-1.33$  V versus RHE, the FE of acetate was 21.2%. Two possible reaction pathways were proposed in this case: One is based on CO dimerization, and the other one is upon CO insertion, highlighting the critical role of CO intermediate formation on active Ag sites. A similar observation was reported in Cu-Zn catalysts (Fig. 6, A and B) for ethanol production (38). By tuning the content of Zn in Zn-Cu alloyed catalysts, the ratio of ethanol versus  $C_2H_4$  FE could be well controlled in the range of 0.48 to 6, suggesting the importance of CO-evolving sites for  $C_{2+}$  oxygenate formation. Formation of alloyed catalysts might induce the strain effect on the matrix material, which may not be desired sometimes. Thus, a direct route toward bimetallic catalysts might be more suitable for some target products. Jaramillo and co-workers (96) constructed a simplified Au-Cu bimetallic system, synthesized by direct deposition of gold NPs onto a polycrystalline Cu foil, to investigate the tandem catalysis effect. The bimetallic Au-Cu exhibited synergistic selectivity and activity toward  $C_{2+}$  alcohols, outperforming pure copper and gold, and Au-Cu alloy. Compared with Cu foil, the bimetallic Au-Cu system showed increased local CO concentration due to the presence of Au NPs (Fig. 6C) that were active for CO generation. Since gold is not active for CO reduction, the enhanced  $C_{2+}$  alcohol production rate on Au-Cu bimetallic catalysts was ascribed to a tandem catalysis mechanism. Specifically, gold NPs could generate a high local CO concentration near the Cu surface. Next, the abundant local CO molecules can be further reduced to  $C_{2+}$  alcohols by Cu.

Selective exposure of crystal facets for electrocatalysts has been demonstrated as an effective and straightforward approach to achieving enhanced FE toward specific ECR products and an important way for fundamental understanding. Simple but scalable synthesis of single-crystal catalysts is challenging. Inspired by the galvanostatic charging-discharging (GCD) procedure for batteries, our group devel-

oped a metal ion cycling method (Fig. 6D) to selectively expose the crystal facet of a Cu catalyst (42). After 100 GCD cycles, a dense Cu nanocube array was formed on the Cu foil with exposed (100) facets (Fig. 6, E to G). The 100-cycle catalyst presented an overall  $C_{2+}$  alcohol FE of more than 30% and a corresponding  $C_{2+}$  alcohol current density of more than  $20 \text{ mA cm}^{-2}$ . However, the 10-cycle Cu with a lower ratio of the (100) facet only offered a  $C_{2+}$  alcohol FE of  $\sim 10\%$ . DFT simulation confirmed that the Cu(100) and stepped (211) facets were more favorable for C—C coupling over Cu(111), as shown in Fig. 6H. A model catalyst, epitaxial Cu film with different exposed facets, has been used to determine the active-site motifs toward  $C_{2+}$  oxygenate production (Fig. 6I) (97). Since it is statistically less likely for a  $CO^*$  dimer to be adjacent to  $H^*$  atoms on a surface with fewer neighbors, lower-coordinated Cu sites could suppress the formation of hydrocarbons and lead to improved  $C_{2+}$  oxygenate FE because it is more difficult to hydrogenate C—C coupled ECR intermediates on its surface (97). In the epitaxial Cu film study, the authors confirmed that the ECR on the Cu(751) facet showed improved oxygenate/hydrocarbon ratio. This enhancement could be ascribed to the surface Cu atom geometry of different Cu facets and the corresponding lower average coordinated number (Fig. 6J), where Cu atom coordinated, respectively, with two, four, and six nearest neighbors on Cu(751), Cu(100), and Cu(111) facets. In situ morphology reconstruction has also been used to improve  $C_{2+}$  oxygenate FE. An active cube-like Cu catalyst was developed by Yang and co-workers (98), which showed improved C—C coupling performance. In detail, monodisperse Cu NPs (6.7 nm) with different loadings were deposited onto carbon paper support as a catalyst for ECR. Obviously, increased FE of  $C_{2+}$  oxygenates was observed with the increase in Cu NP loading. It was shown that densely packed Cu NPs under high loading conditions underwent in situ morphological transformation during ECR, in which cube-like morphologies were lastly formed (Fig. 6K). This newly formed structure was found to be more electrocatalytically active. Tafel analysis suggested that CO dimerization was the rate-determining step for  $C_2$  product formation, whereas that of *n*-propanol showed a discrete pathway in this catalytic system. Nanodendritic copper is another example that shows the importance of morphology control for  $C_{2+}$  oxygenate production (99). Briefly, the total FE of the well-defined copper nanodendrite (Fig. 6L) for  $C_{2+}$  alcohol was about 25% at  $-1.0$  V versus RHE. An impressive *n*-propanol FE of 13% could be achieved at  $-0.9$  V. Considering the high activity of Cu atom, copper-based catalysts always suffer from structural degradation during ECR, especially at high overpotential, which, in turn, leads to poor stability. However, such a nanodendritic copper exhibited good stability for alcohol production, showing an alcohol FE of  $\sim 24\%$  over 6 hours.

Defects of electrocatalysts, such as atom vacancies and dopants, show the possibility of adsorbing unconventional ECR intermediates and, thus, selectively enhancing the corresponding pathway toward oxygenates (29, 43, 100). Taking  $*C_2H_3O$  as an example, which is the potential penultimate intermediate for ethylene and ethanol production, Sargent and co-workers (43) studied the role of defects in a core-shell Cu electrocatalyst in detail. They theoretically showed that the reaction energy barriers for ethylene and ethanol formation were similar in the early C—C coupling stage (0.5-V overpotential) (Fig. 7A). Under such a condition, the introduction of copper vacancy would slightly increase the energy barrier for ethylene formation, yet it showed no influence on the ethanol generation (Fig. 7B). However, as shown in Fig. 7C, copper catalysts with vacancy and subsurface sulfur dopant



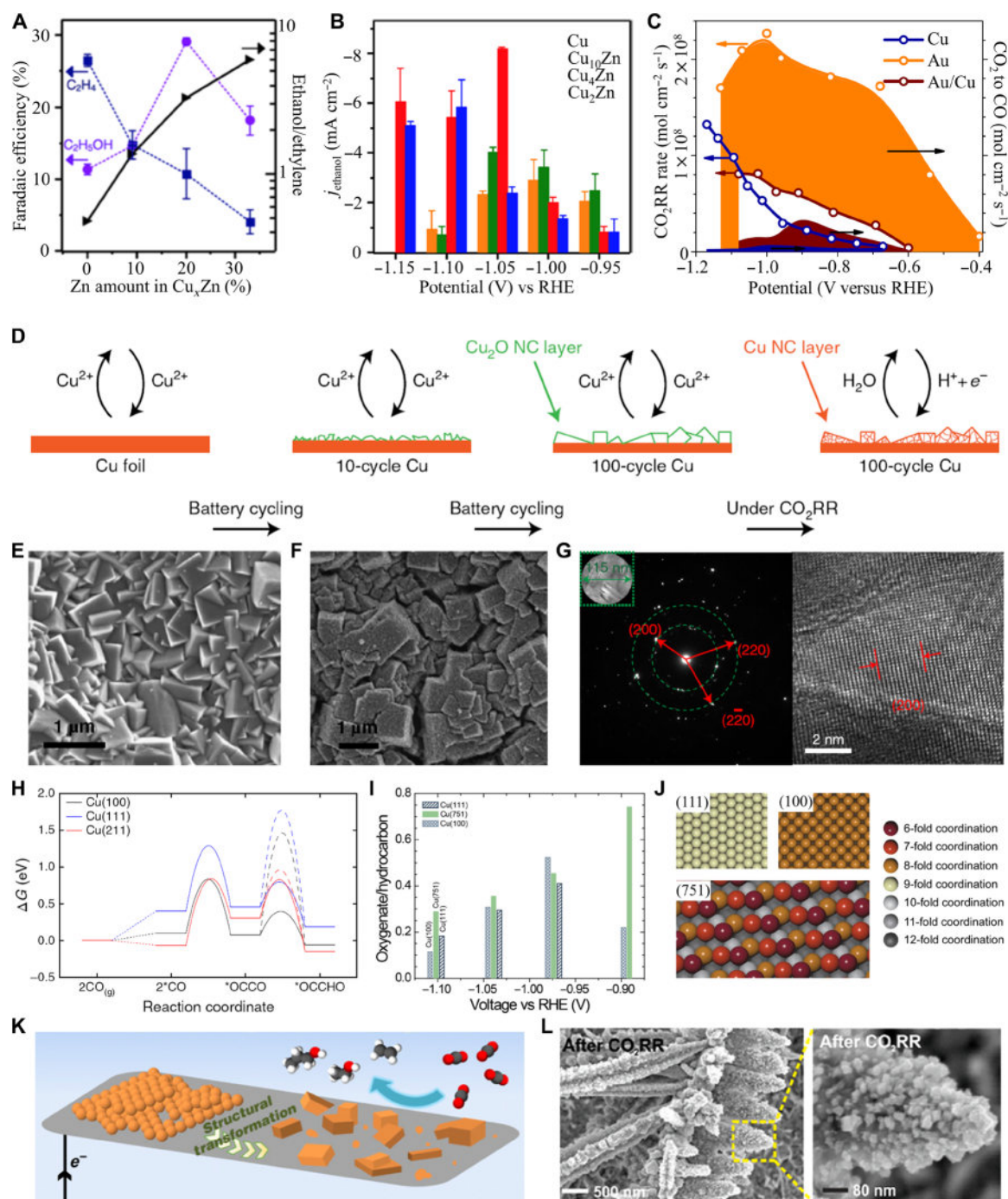


**Fig. 6. Alloy, morphology, and structure effects on ECR catalysts for efficient  $C_2+$  oxygenate production.** (A to C) Alloy effects. (A) Maximum FE of ethanol and  $C_2H_4$  and the FE ratio of ethanol and ethylene on various Cu-Zn alloys. (B) Partial current density of ethanol on various Cu-Zn alloys. (A) and (B) are reproduced with permission from the American Chemical Society (38). (C)  $CO_2$  reduction and CO evolution rates on gold, copper, and the Au-Cu bimetallic system. Reproduced with permission from the Nature Publishing Group (96). (D to L) Morphology or structure effects. (D) Schematic illustration of metal ion cycling method. (E and F) SEM images of 100-cycle Cu before (E) and after (F) the prereluction under ECR conditions. (G) TEM and selected-area electron diffraction suggested that Cu(100) were exposed and (H) free energy for  $*OCCO$  and  $*OCCHO$  formation on Cu(100), Cu(111), and Cu(211) facets. (D) to (G) are reproduced with permission from the Nature Publishing Group (42). (I) Ratio of oxygenates and hydrocarbons as a function of potential on Cu(111), Cu(751), and Cu(100). (J) Coordination numbers for Cu(111), Cu(100), and Cu(751). (I) and (J) are reproduced with permission from the National Academy of Sciences (97). (K) Scheme of the transformation process from Cu NPs to cubic-like copper. Reproduced with permission from the National Academy of Sciences (98). (L) SEM images of nanodendritic copper before and after ECR. Reproduced with permission from the American Chemical Society (99).

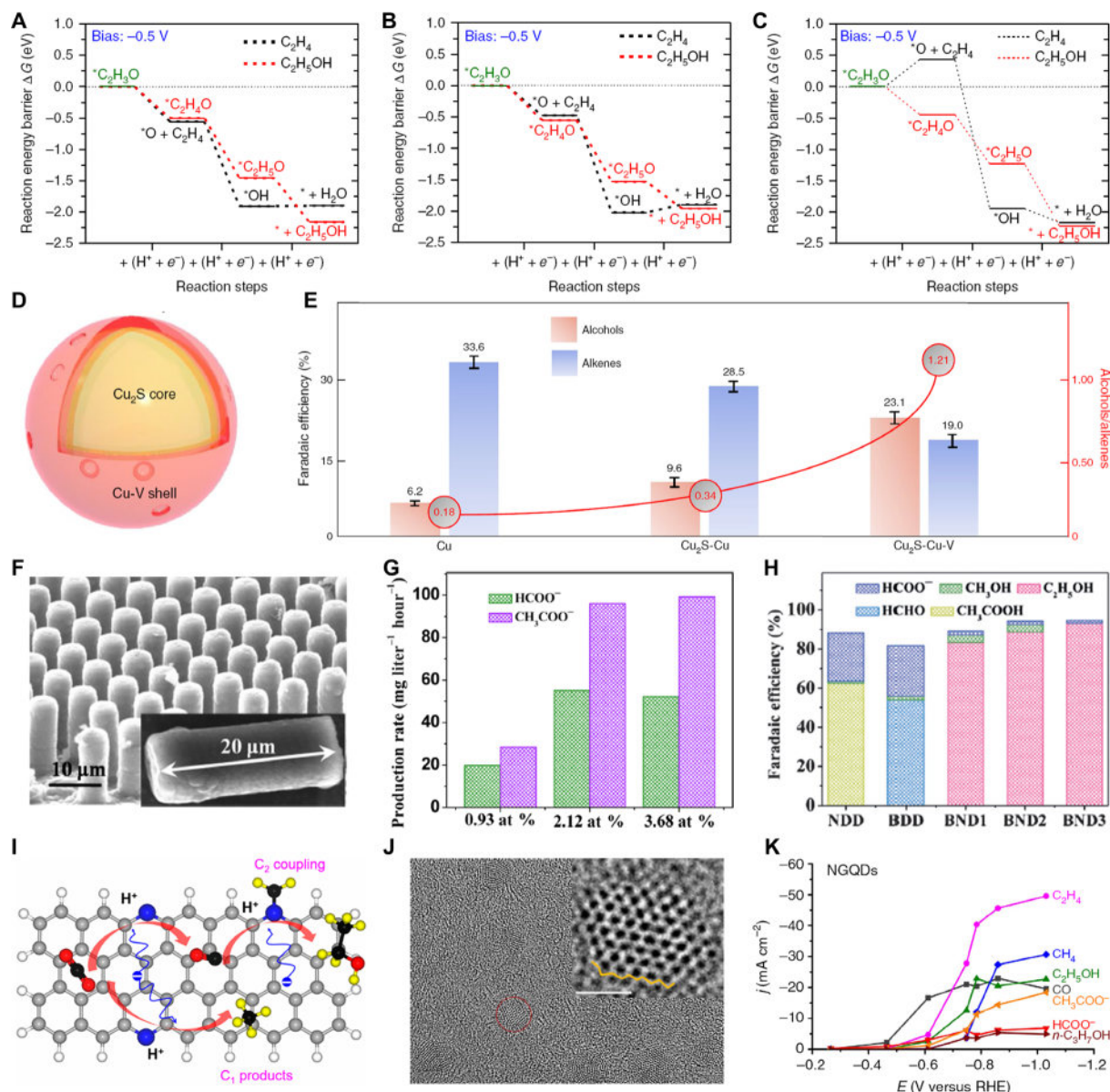


**Fig. 7. Defect engineering for  $C_2+$  oxygenate production.** (A to C) Gibbs free energy from  $*C_2H_3O$  to ethylene and ethanol for copper, copper with vacancy, and copper with copper vacancy and subsurface sulfur. (D) Schematic illustration of the  $Cu_2S-Cu-V$  catalyst. (E) FE of  $C_2+$  alcohols and ethylene, as well as the FE ratio of alcohols to alkenes. (A) to (E) are reproduced with permission from the Nature Publishing Group (43). (F) SEM image of NDD. (G) Production rates of acetate and formate on NDD with different nitrogen contents. at %, atomic %. (F) and (G) are reproduced with permission from the American Chemical Society (29). (H) FEs for NDD, BDD, and BNDs at  $-1.0$  V. Reproduced with permission from John Wiley and Sons (102). (I) Schematic illustration of the active sites for C—C coupling in NGQDs. (I) is reproduced with permission from the American Chemical Society (103). (J) TEM image of NGQDs. Scale bars, 1 nm. (K) Partial current densities for various products using NGQDs. (J) and (K) are reproduced with permission from the Nature Publishing Group (37).

could significantly increase the energy barrier for the ethylene route, making it thermodynamically unfavorable. However, such a modification showed a negligible effect on the ethanol pathway. This phenomenon was further experimentally verified. A core-shell structured  $Cu_2S-Cu$  with abundant surface vacancies ( $Cu_2S-Cu-V$ ; Fig. 7D) was synthesized. The ratio of alcohol to ethylene increased from 0.18 on bare Cu NPs to 0.34 on vacancy-free  $Cu_2S-Cu$  and then to 1.21 on  $Cu_2S-Cu-V$ , although the total FE of  $C_2+$  products for all catalysts remained similar (Fig. 7E). This observation indicated that the promotion of alcohol selectivity was associated with the suppression of

ethylene production, consistent with the DFT result. In addition, defect engineering plays a more important role for metal-free carbon catalyst since pure carbon materials are inactive for ECR. Dopants such as nitrogen and boron have been used to alter the electronic structure of a carbon-based catalyst (31, 43, 100). For example, nitrogen-doped nanodiamond (NDD) film on silicon substrate was devolved by Quan *et al.* (29) for selective acetate production from ECR (Fig. 7F). The acetate onset potential was as low as  $-0.36$  V versus RHE using an NDD catalyst, and the FE for acetate was more than 75% in a potential range from  $-0.8$  to  $-1.0$  V versus RHE. To understand the

origin of such an impressive improvement, NDD/Si electrodes with different nitrogen contents or nitrogen species were prepared and investigated (Fig. 7G). The authors concluded that the superior performance of the NDD/Si catalyst for ECR could be attributed to its high overpotential for hydrogen evolution and N doping, where N-sp<sup>3</sup>C species was highly active for acetate production. Electrokinetic data and in situ infrared spectrum revealed that the main pathway for acetate formation might be  $\text{CO}_2 \rightarrow * \text{CO}_2^- \rightarrow *(\text{COO})_2 \rightarrow \text{CH}_3\text{COO}^-$ . Besides nitrogen, boron is another well-explored heteroatom to regulate the electronic structure of nanodiamond. However, boron-doped nanodiamond (BDD) preferentially reduced  $\text{CO}_2$  to formaldehyde or formate (101). Furthermore, Quan and co-workers (102) demonstrated that boron and nitrogen co-doped nanodiamond (BND) showed synergistic effect on ECR, which could overcome the limitation of BDD and then selectively produce ethanol. BND1, BND2, and BND3 catalysts with different nitrogen contents and similar boron doping levels were prepared. As shown in Fig. 7H, the highest selectivity of ethanol up to 93% could be achieved on the BND3 catalyst at  $-1.0$  V versus RHE, which has the highest nitrogen doping. Theoretical calculation illustrated that the C–C coupling process on BND was thermodynamically favorable, where the boron atom promoted the capture of  $\text{CO}_2$  and nitrogen dopant facilitated the hydrogenation of intermediate toward ethanol. Although heteroatom-doped nanodiamond was capable of converting  $\text{CO}_2$  into multicarbon oxygenates with high selectivity, its ECR activity is very limited because of the slow charge transfer process (current density is less than  $2 \text{ mA cm}^{-2}$ ). Graphene-based material might be a potential solution to overcome the shortcomings of diamond-based catalysts. Theoretically, the edge pyridinic N sites in the graphene layer have been taken as the active sites for C–C coupling (103). This is due to the fact that the presence of pyridinic N at edge sites could convert  $\text{CO}_2$  into CO, which can be further coupled into  $\text{C}_{2+}$  molecule (Fig. 7I). For example, the  $*\text{C}_2\text{O}_2$  intermediate could be stabilized in nitrogen-doped carbon in which the two C atoms are bonded to the pyridinic N and its adjacent C atom, respectively (103). The theoretical prediction was then validated using nitrogen-doped graphene quantum dot (NGQD) catalysts (31). After the pulverization of nitrogen-doped graphene sheets (1 to 3  $\mu\text{m}$ ) (Fig. 7J), 1- to 3-nm NGQDs were obtained in which the density of pyridinic N at edge sites was increased by three orders of magnitude. At  $-0.78$  V versus RHE, the maximum FE for  $\text{C}_{2+}$  oxygenates could reach up to 26%. In addition, as shown in Fig. 7K, the partial current density for  $\text{C}_{2+}$  oxygenates is close to  $40 \text{ mA cm}^{-2}$  at  $-0.86$  V versus RHE, which is much higher than that of the modified nanodiamond. In comparison, N-free graphene quantum dots and N-doped graphene oxide, which show much lower edge site pyridinic N, primarily yielded  $\text{H}_2$ , CO, and formate.

## DESIGN OF THE ELECTROREDUCTION CELL

Beyond electrocatalysts, electrode and catalytic reactor architecture design present another effective route to boost the ECR performance, especially for production rate and energy efficiency. Significant improvements have been made on design and fabrication of novel electroreduction systems to achieve highly efficient  $\text{C}_{2+}$  production. In this section, we will discuss the ECR electrode/reactor design in detail.

### Electrolyzer design

H-type cells are extensively used in lab-scale tests, considering their facile assembly, easy operation, and low cost. The cells are equipped

with independent cathode and anode chambers that are connected by an ion-exchange membrane (104, 105). The primary disadvantage of this H-type cell is the low  $\text{CO}_2$  solubility in aqueous electrolyte, which is only  $0.034 \text{ M}$  under ambient conditions, leading to limited  $\text{CO}_2$  reduction current densities of  $j < 100 \text{ mA cm}^{-2}$  (64). Moreover, other intrinsic drawbacks, including a limited electrode surface area and a large interelectrode distance, have failed to meet the growing research requirements (105, 106). For  $\text{C}_{2+}$  product generation, H-type cells usually show low selectivity under high overpotentials, e.g., 32% for ethylene at  $-0.98$  V versus RHE (107), 13.1% for *n*-propanol at  $-0.9$  V versus RHE (99), and 20.4% for ethanol at  $-0.46$  V versus RHE (108), due to the seriously competitive hydrogen evolution.

To address the above issues, the flow reactor was proposed (15, 109). In flow cells, gaseous  $\text{CO}_2$  stream can be directly used as feedstock at cathode, thus leading to significantly improved mass diffusion and production rate (104, 110). Figure 8A shows the typical architecture of a flow cell, where a polymer electrolyte membrane (PEM) served as the electrode separator that is sandwiched between two flow channels. The catalyst is immobilized onto a gas diffusion electrode (GDE) to serve as the cathode electrode, in which gaseous  $\text{CO}_2$  is directly fed. The catholyte, such as  $0.5 \text{ M KHCO}_3$ , is continuously flowed within the thin layer between the catalyst electrode and PEM. In addition, the anode side is typically circulated with an aqueous electrolyte for oxygen evolution reaction (43, 110). Compared with H-type cells, these membrane-based flow cells show much superior ECR performance. For example, Sargent and co-workers (43) evaluated the ECR performance of the  $\text{Cu}_2\text{S}$ -Cu-V catalyst in both H-type cell and flow cell, as depicted in Fig. 8 (B to E). Using H-type cells, the maximum FE for  $\text{C}_{2+}$  products was 41% with a total current density of  $\sim 30 \text{ mA cm}^{-2}$  under  $-0.95$  V versus RHE. However, the FE for  $\text{C}_{2+}$  products increased to 53% with a total current density easily exceeding  $400 \text{ mA cm}^{-2}$  under  $-0.92$  V versus RHE in a flow system. Such a significant performance improvement using the flow reactor can be ascribed to the enhanced  $\text{CO}_2$  diffusion and suppressed side reactions, mainly originating from the local gas-electrolyte-catalyst triple-interface architecture.

The zero gap cell is another emerging class of electrolyzers, which further removes the flow channels in flow cells and presses two electrodes together with an ion-exchange membrane in between. This configuration could significantly decrease mass transfer and electron transfer resistance and thus improve energy efficiency, making it more feasible in practical applications (110). The reactants fed to the cathode can be either  $\text{CO}_2$ -saturated catholyte or humidified  $\text{CO}_2$  stream. Water vapor or aqueous electrolyte is mandatorily fed to the anode for proton release to compensate the charge for the  $\text{CO}_2$  reduction species (111). Gutiérrez-Guerra *et al.* (109) evaluated the performance of the Cu-AC hybrid catalyst in the zero gap cell and reported that acetaldehyde is the main product with a high selectivity of 60%. As another advantage of this device, it is very easy to pressurize the reactant flow and significantly enhance the local  $\text{CO}_2$  concentration, thus resulting in large current densities and high reaction rates (110). However, the accelerated ion exchange rate in zero gap cells tends to acidify the catholyte, shifting the reaction toward  $\text{H}_2$  evolution instead of  $\text{CO}_2$  reduction (112). To tackle this problem, Zhou and co-workers (112, 113) inserted a buffer layer with a circulating aqueous electrolyte between the cathode and membrane to maintain the proper pH near the cathode for  $\text{CO}_2$  reduction reaction. Although various  $\text{C}_{2+}$  products were detected on the basis of the zero gap cells, including acetone, ethanol, and *n*-propanol, the FEs are still relatively low. Most



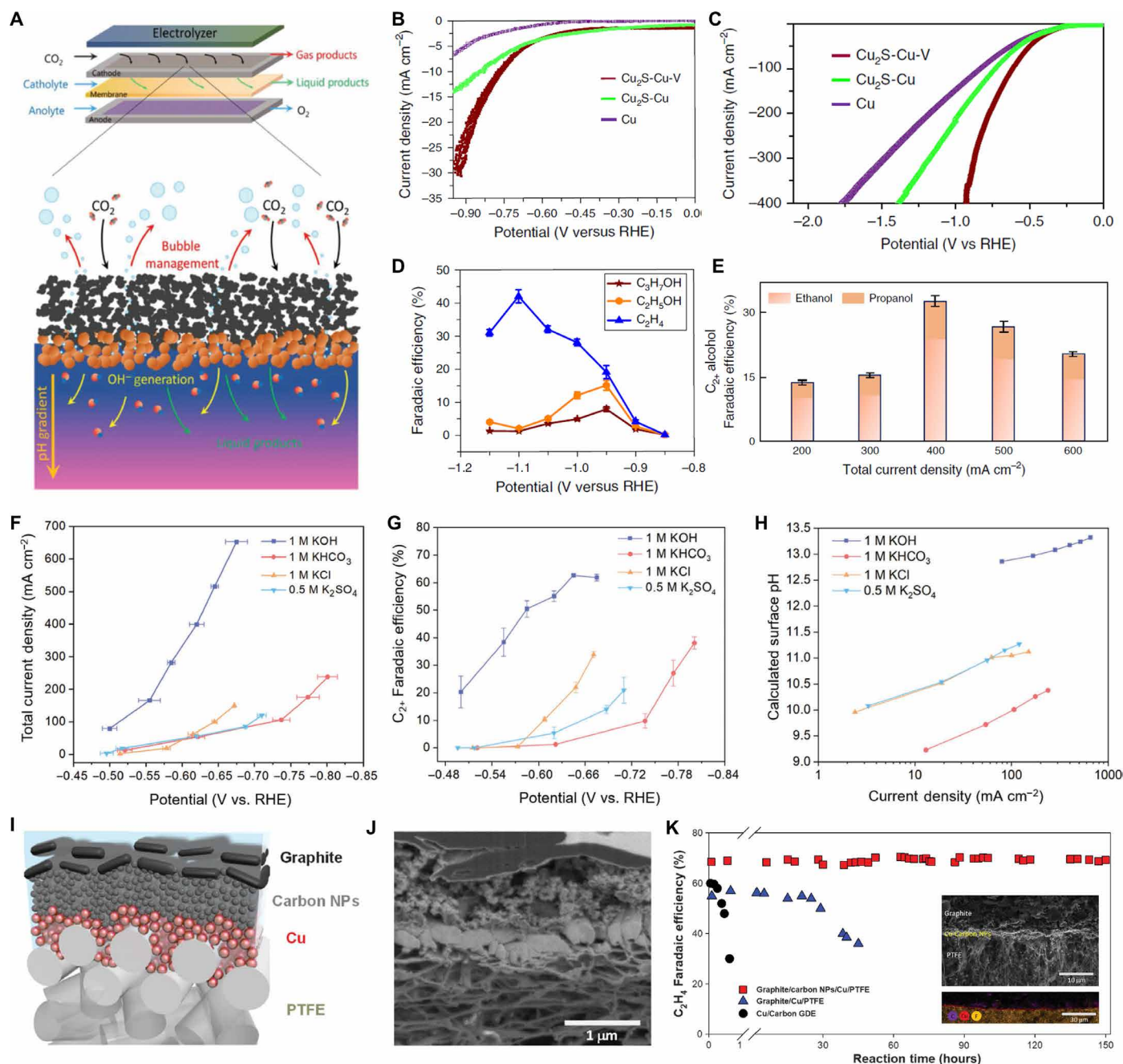


**Fig. 8. Electrolyzer and electrode engineering for C<sub>2+</sub> production.** (A) A diagram of the flow electrolyzer with a zoomed-in schematic of the electrode-electrolyte interface. (A) is reproduced with permission from John Wiley and Sons (30). (B to E) Comparison of ECR performance using H-type cell and flow cell. (B) to (E) are reproduced with permission from the Nature Publishing Group (43). (F to H) Different electrolytes applied in flow cells versus the ECR performance. (F) to (H) are reproduced with permission from John Wiley and Sons (30). (I to K) Structure and stability performance of the polymer-based gas diffusion electrode. (I) to (K) are reproduced with permission from AAAS (33).

reported studies always focus on C<sub>1</sub> products that involve fewer numbers of proton and electron transfers during the reduction reaction. Therefore, the feasibility of the zero gap cell for C<sub>2+</sub> products is still under debate (110).

Moreover, microfluidic electrolytic cells (MECs) are a kind of highly attractive electrolyzer configuration developed by Kenis and co-workers (39, 114). In this device, the membrane is replaced by a

thin space (<1 mm in thickness) filled with flowing electrolyte stream to separate the anode and cathode. The CO<sub>2</sub> molecules could quickly diffuse into the electrode-electrolyte interface near cathode, and the two fixed GDEs are flushed by flowing electrolyte. Compared to membrane-based flow cells, MECs not only avoid the high membrane cost but also mitigate water management, which particularly refers to the anode dry-out and cathode flooding when operated

at high current densities owing to the osmotic drag of water molecules along with proton transport from anode to cathode across the membrane (115). As far as we know, despite the noticeable merits and achievements, a minimal number of studies have achieved  $C_{2+}$  products in the original MECs. This is probably caused by the “floating” effect that protons formed in the anode are easily drained from the cathode vicinity or washed away by the flowing electrolyte, rather than participating in the multiple proton required  $C_{2+}$  formation reaction. The speculation could be confirmed by the following instance. In 2016, Kenis and co-workers (31) reported the successful reduction of  $CO_2$  to  $C_{2+}$  products on a modified and membrane-containing MEC, in which NGQDs could reduce  $CO_2$  molecules to  $C_{2+}$  with 55% FE (31% for ethylene, 14% for ethanol, 6% for acetate, and 4% for *n*-propanol) at an applied potential of  $-0.75$  V versus RHE in 1 M KOH solution. It is important to point out that an electrolyte environment could significantly affect the product selectivity as well. For example, Jiao and co-workers (30) synthesized a nanoporous Cu catalyst and then tested its ECR performance using different electrolytes ( $KHCO_3$ , KOH,  $K_2SO_4$ , and KCl) in a membrane-based MEC. They revealed that the  $CO_2$  reduction in alkaline electrolyte (KOH) exhibits the highest  $C_{2+}$  selectivity and current density, as shown in Fig. 8 (F and G). At  $-0.67$  V versus RHE in 1 M KOH electrolyte, the obtained FE for  $C_{2+}$  reaches up to 62% with a partial current density of  $653\text{ mA cm}^{-2}$ , which is among the highest current densities that have ever been reported in electrochemical  $CO_2$  reductions toward  $C_{2+}$  products. Ethylene (38.6%), ethanol (16.6%), and *n*-propanol (4.5%) are the main  $C_{2+}$  products with a small amount of acetate. They also pointed out that there is a strong correlation between the calculated surface pH and FE for  $C_{2+}$  products: The higher the surface pH, the higher current densities and  $C_{2+}$  products yield, as depicted in Fig. 8H. The theoretical calculation proposed that the near-surface  $OH^-$  ions could strongly facilitate C—C coupling (31).

In addition to the electrolyzer configuration, the electrolyte applied in different electrolyzers could also substantially alter the final ECR products. As we mentioned above, highly alkaline KOH solutions are always used in flow cells with excellent performance rather than in H-type cells. It is ascribed to the fact that KOH electrolyte could provide higher electrolyte conductivity, decrease ohmic resistance between the thin electrolyte coating on catalyst and bulk electrolyte, and further decrease the required overpotentials for  $C_{2+}$  formation (31). The DFT results further confirm that the presence of  $OH^-$  ions could lower the energy barrier for CO dimerization, thus boosting the  $C_{2+}$  formation and suppressing the competition from  $C_1$  and  $H_2$  formation (30, 33). However, alkaline KOH could not be used as electrolyte in H-type cells. This is because  $CO_2$  streams will rapidly react with KOH solutions and lastly create a bicarbonate solution with neutral pH in H-type cells (30). In flow cells, however, once the  $CO_2$  diffuses through the GDE, the  $CO_2$  molecules will be consumed at the triple boundary phase ( $CO_2$ -catalyst-electrolyte) to form reduced products immediately. Besides, the poor buffering capacity of the electrolyte is able to rapidly increase the pH around the electrode in stationary electrolyzer configurations, whereas the flowing electrolyte will refresh the surface and minimize the pH fluctuation in the electrolyte (33, 116).

As aforementioned that ECR is a diffusion-controlled reaction, high reaction pressure could also significantly enhance the bulk and interface  $CO_2$  concentration. The common high-pressure reactors are similar to the stainless steel autoclave, in which high-pressure  $CO_2$  (up to 60 atm) could be introduced into the cell, leading to a remarkable increase in both the FE and the current density of  $C_{2+}$

(117, 118). Sakata and co-workers (119) showed that the current density could be improved to  $163\text{ mA cm}^{-2}$  under 30 atm on a Cu electrode with ethylene as the major product. Many metal catalysts (e.g., Fe, Co, and Ni), with no activity for  $C_{2+}$  production at ambient pressure, could reduce  $CO_2$  to ethylene, ethane, propane, and other high-order  $C_{2+}$  products at elevated pressures. It has been demonstrated that the selectivity of the products markedly depends on the  $CO_2$  pressure in the manner of altering  $CO_2$  availability at the electrode surface (117, 120). The main reduced products are altered from  $H_2$  to hydrocarbons ( $C_{2+}$  included) and lastly to CO/HCOOH with increased  $CO_2$  pressure. Notably, the  $CO_2$  pressure should be carefully monitored because excessive high or low  $CO_2$  pressures would induce superfluous or limited  $CO_2$  diffusion rate, which tends to favor the production of CO/HCOOH or  $H_2$ . Only a compatible amount of intermediate CO and current density that generated on the electrode surface could facilitate the C—C coupling reaction and enhance  $C_{2+}$  product selectivity (119).

### Structure of a GDE

Designing a novel electrode with advanced structures is another important direction to enhance the selective  $C_{2+}$  production. In early stage, the working electrodes are nonporous metal foils and suffer from sluggish mass transfer (26, 105). As a result, GDE was proposed to alleviate the poor cell performance by providing hydrophobic channels that facilitate  $CO_2$  diffusion to catalyst particles (121). The conventional GDE usually comprises a catalyst layer (CL) and a gas diffusion layer (GDL), as shown in the lower part of Fig. 8A (30, 33). The gas-liquid-catalyst interface formed in GDE is crucial to improve the cell performance. The GDL assembled with porous materials (typically carbon paper) could provide abundant  $CO_2$  pathways and ensure rapid electrolyte diffusion rate. It also acts as a low-resistance transportation medium for protons, electrons, and reduction products from the CL into the electrolyte (121). Drop casting, airbrushing, and electrodeposition are the common technologies for preparation of GDEs (122). Catalysts assembled with GDEs have been intensively investigated in  $CO_2$  electroreduction to  $C_{2+}$  products. Notably, the aforementioned flow cells with favorable performance are all coupled with GDEs. As early as 1990, Sammells and co-workers (123) reported that Cu-coated GDEs achieved high FE of 53% for ethylene with a high density of  $667\text{ mA cm}^{-2}$ . Enhancing the selectivity of ethylene and ethanol is a major challenge that is always coproduced on Cu-based catalysts because of their very similar mechanistic reaction pathways. Moreover, it is important to point out that the elevated productivity and selectivity of ethylene compared to ethanol have been observed on Cu-based GDE (25, 36). Gewirth and co-workers (36) showed an excellent FE of 60% for ethylene and a suppressed FE for ethanol of 25% on electrodeposited Cu-Ag GDE, when the total current density reached  $\sim 300\text{ mA cm}^{-2}$  at  $-0.7$  V versus RHE. It is a rare work that achieved such a high selectivity at a large current density. This finding suggests that a GDE-incorporated electrode provides a promising avenue for tuning the reaction pathways, in which the selectivity of reduced products can be obtained at high current densities.

The stability of GDEs is also a significant issue that should be addressed because stable long-term operation is essential to realize practical application for flow cells. Despite the outstanding  $CO_2$ -to- $C_{2+}$  performance achieved with GDEs, the stability is still poor due to the weak mechanical adhesion of the catalyst, GDL, and binder layers (77, 124). The carbon surface of GDL might change from hydrophobic to hydrophilic during the electrochemical reaction due to the oxidation reaction that occurred at elevated overpotentials, which leads to

the flooding in GDL and obstructed CO<sub>2</sub> diffusion pathways (33). To solve this problem, researchers integrated hydrophobic scaffold of polytetrafluoroethylene (PTFE) into GDEs. Compared to hydrophilic Nafion, a hydrophobic PTFE layer renders a superior long-term stability (33). Sargent and co-workers (33) assembled a Cu catalyst between the separated PTFE and carbon NPs, in which the hydrophobic PTFE layer could immobilize the NPs and graphite layers, thus constructing a stable electrode interface (Fig. 8, I and J). As a result, the FE for ethylene production was increased to 70% in 7 M KOH solution at current densities of 75 to 100 mA cm<sup>-2</sup>. The life span of this flow reactor was extended to more than 150 hours with negligible loss in ethylene selectivity, which is 300-fold longer than traditional GDEs, as shown in Fig. 8K. Such a sandwich structure has been demonstrated to be an excellent GDE design. For example, Cui and co-workers (124) designed a trilayer structure with an active electrode layer clipped by two hydrophobic nanoporous polyethylene films. The outer hydrophobic layers could slow down the electrolyte flux from the bulk solution, leading to stable, high local pH around the working electrode. Optimization of the interlayer space, which can improve CO<sub>2</sub> transport and adsorption, is also important in such a design (124). Recently, carbon nanotubes have also been integrated into the GDEs because of their high porosity, good conductivity, and hydrophobicity, which could facilitate electron and mass transportation (77).

Despite the exciting progresses on ECR, strategies for low-cost, large-scale C<sub>2+</sub> product generation are rarely present (125). At this stage, the challenges and opportunities are concurrent to understand the reaction mechanisms of ECR and commercialize this promising technology.

## SUMMARY AND OUTLOOK

As an elegant solution to close the carbon loop and store intermittent renewable energy, such as wind and solar, substantial progresses have been made to achieve efficient CO<sub>2</sub> conversion in the past decades. While the understanding of the processes associated with ECR has come a long way since its early days (126), the C—C coupling via ECR toward C<sub>2+</sub> products is still far from ready for practical application. In this review, we took a detailed look at the current strategies that can promote the selectivity and production rate for C<sub>2+</sub> products via ECR, including fine-catalyst tuning, electrolyte effects, electrochemical conditions, and electrochemical electrode/reactor design.

Despite all the effort put into ECR, there are still many problems with the current catalysts and ECR system that must be addressed before commercializing ECR. First, as the dominating catalyst to realize efficient C—C coupling, Cu suffers from serious stability issues, especially in aqueous electrolyte, and can rarely survive for 100 hours due to their high atom mobility, particle aggregation, and structure deterioration under ECR conditions. Thus, how to achieve long-period stability using a Cu-based catalyst is still an open challenge. Anchoring the Cu-based catalyst on specific support with strong interaction might be a reliable strategy to preserve the catalyst structure/morphology and thus provides enhanced life span. Furthermore, using a polymer membrane electrolyte to replace the aqueous solution during ECR can probably further improve the stability of the Cu-based catalyst. In addition, from the perspective of catalysts, in situ/in operando characterization techniques and theoretical modeling should also be used to monitor and understand the catalyst performance decay, thus, in turn, suppressing the degradation and poisoning of catalyst to the

lowest levels. Another important issue of ECR catalysts that should be addressed is to make the synthesis protocol viable for mass production. To this end, streamlining the synthetic procedures using widely available feedstocks is preferred.

Second, the generated C<sub>2+</sub> oxygenated from ECR are usually mixed with solutes (e.g., KHCO<sub>3</sub> and KOH) in the electrolyte for traditional H- or flow-cell reactors, which, however, requires extra separation and concentration processes to recover pure liquid fuel solutions in practical applications. At the same time, the evolved C<sub>2+</sub> hydrocarbons are also mixed with H<sub>2</sub> and residual CO<sub>2</sub>. Thus, a costly separation process is indispensable for current ECR technology, which further hinders ECR from practical application. Therefore, how to directly and continuously produce pure liquid fuel solutions and pure gas hydrocarbons, particularly with high product concentrations, is highly desirable for the practical deployment of ECR. We thus predict the rising importance of direct generation of pure products via ECR in the near future, which may take the ECR technology much closer to market (127).

Third, while the formation of C—O and C—H bonds, such as ethanol, acetic acid, and ethylene, in ECR technology has been heavily studied, exploration of other types of products is also important for ECR technology and shows economical interest. For example, recently, Han and co-workers (128) reported the production of 2-bromoethanol by ECR. The in situ formation of C—Br bond transforms the product from ethanol to 2-bromoethanol, which is an important building block in chemical and pharmaceutical synthesis and shows higher added value. Thus, beyond the current well-studied C<sub>2+</sub> products, we believe that targeting of other rarely explored products such as oxalic acid (129) and synthesis of more complex C<sub>2+</sub> molecules such as cyclic compounds is another promising route for future ECR research.

Last but not least, novel electrode and reactor designs such as waterproof GDE, liquid-flow cells, and PEM cell should be widely adopted to boost the ECR production rate to commercial level (>200 mA cm<sup>-2</sup>). However, the large discrepancy in electrocatalytic activity is always observed when electrocatalysts are applied to the full cell test. Therefore, more systematic studies should be performed to minimize the gap between half-cell studies and full-cell device application to bring the ECR from lab-scale test to practical use.

In summary, electrochemical CO<sub>2</sub> reduction offers good opportunity for us to deal with the environmental issue from greenhouse gases emitted by human activities. It also shows the possibility to achieve clean fuels and chemicals using renewable energy. While many challenges remain for ECR technology at the current stage, especially for the C—C coupling process, it is believed that with continued research and development on both catalyst optimization and cell perfection, the perspective of a real-world CO<sub>2</sub> electrolysis for clean fuel and chemicals will be realized in the near future.

## REFERENCES AND NOTES

1. S. Solomon, G.-K. Plattner, R. Knutti, P. Friedlingstein, Irreversible climate change due to carbon dioxide emissions. *Proc. Natl. Acad. Sci. U.S.A.* **106**, 1704–1709 (2009).
2. J.-P. Gattuso, A. Magnan, R. Billé, W. W. L. Cheung, E. L. Howes, F. Joos, D. Allemand, L. Bopp, S. R. Cooley, C. M. Eakin, O. Hoegh-Guldberg, R. P. Kelly, H.-O. Pörtner, A. D. Rogers, J. M. Baxter, D. Laffoley, D. Osborn, A. Rankovic, J. Rochette, U. R. Sumaila, S. Treyer, C. Turley, Contrasting futures for ocean and society from different anthropogenic CO<sub>2</sub> emissions scenarios. *Science* **349**, aac4722 (2015).
3. M. Mikkelsen, M. Jørgensen, F. C. Krebs, The teraton challenge. A review of fixation and transformation of carbon dioxide. *Energy Environ. Sci.* **3**, 43–81 (2010).
4. D. D. Zhu, J. L. Liu, S. Z. Qiao, Recent advances in inorganic heterogeneous electrocatalysts for reduction of carbon dioxide. *Adv. Mater.* **28**, 3423–3452 (2016).



5. K. K. Sakimoto, A. B. Wong, P. Yang, Self-photosensitization of nonphotosynthetic bacteria for solar-to-chemical production. *Science* **351**, 74–77 (2016).
6. B. Obama, The irreversible momentum of clean energy. *Science* **355**, 126–129 (2017).
7. S. Chu, Y. Cui, N. Liu, The path towards sustainable energy. *Nat. Mater.* **16**, 16–22 (2017).
8. N. S. Lewis, Research opportunities to advance solar energy utilization. *Science* **351**, aad1920 (2016).
9. H.-R. M. Jhong, S. Ma, P. J. A. Kenis, Electrochemical conversion of CO<sub>2</sub> to useful chemicals: Current status, remaining challenges, and future opportunities. *Curr. Opin. Chem. Eng.* **2**, 191–199 (2013).
10. K. Jiang, S. Siahrostami, A. J. Akey, Y. Li, Z. Lu, J. Lattimer, Y. Hu, C. Stokes, M. Gangishetty, G. Chen, Y. Zhou, W. Hill, W.-B. Cai, D. Bell, K. Chan, J. K. Nørskov, Y. Cui, H. Wang, Transition-metal single atoms in a graphene shell as active centers for highly efficient artificial photosynthesis. *Chem* **3**, 950–960 (2017).
11. P. De Luna, C. Hahn, D. Higgins, S. A. Jaffer, T. F. Jaramillo, E. H. Sargent, What would it take for renewably powered electrosynthesis to displace petrochemical processes? *Science* **364**, eaav3506 (2019).
12. J. B. Greenblatt, D. J. Miller, J. W. Ager, F. A. Houle, I. D. Sharp, The technical and energetic challenges of separating (photo) electrochemical carbon dioxide reduction products. *Joule* **2**, 381–420 (2018).
13. O. S. Bushuyev, P. De Luna, C. T. Dinh, L. Tao, G. Saur, J. de Lagamaat, S. O. Kelley, E. H. Sargent, What should we make with CO<sub>2</sub> and how can we make it? *Joule* **2**, 825–832 (2018).
14. K. Li, B. Peng, T. Peng, Recent advances in heterogeneous photocatalytic CO<sub>2</sub> conversion to solar fuels. *ACS Catal.* **6**, 7485–7527 (2016).
15. S. Verma, B. Kim, H.-R. M. Jhong, S. Ma, P. J. A. Kenis, A gross-margin model for defining technoeconomic benchmarks in the electroreduction of CO<sub>2</sub>. *ChemSusChem* **9**, 1972–1979 (2016).
16. R. Kortlever, J. Shen, K. J. P. Schouten, F. Calle-Vallejo, M. T. M. Koper, Catalysts and reaction pathways for the electrochemical reduction of carbon dioxide. *J. Phys. Chem. Lett.* **6**, 4073–4082 (2015).
17. M. Gattrell, N. Gupta, A. Co, A review of the aqueous electrochemical reduction of CO<sub>2</sub> to hydrocarbons at copper. *J. Electroanal. Chem.* **594**, 1–19 (2006).
18. J. Durst, A. Siebel, C. Simon, F. Hasché, J. Herranz, H. A. Gasteiger, New insights into the electrochemical hydrogen oxidation and evolution reaction mechanism. *Energy Environ. Sci.* **7**, 2255–2260 (2014).
19. A. D. Handoko, F. Wei, B. S. Yeo, Z. W. Seh, Understanding heterogeneous electrocatalytic carbon dioxide reduction through operando techniques. *Nat. Catal.* **1**, 922–934 (2018).
20. A. A. Peterson, F. Abild-Pedersen, F. Studt, T. F. Rossmeisl, J. K. Nørskov, How copper catalyzes the electroreduction of carbon dioxide into hydrocarbon fuels. *Energy Environ. Sci.* **3**, 1311–1315 (2010).
21. X. Zheng, Y. Ji, J. Tang, J. Wang, B. Liu, H.-G. Steinrück, K. Lim, Y. Li, M. F. Toney, K. Chan, Y. Cui, Theory-guided Sn/Cu alloying for efficient CO<sub>2</sub> electroreduction at low overpotentials. *Nat. Catal.* **2**, 55–61 (2019).
22. X. Zheng, P. De Luna, F. P. G. de Arquer, B. Zhang, N. Becknell, M. B. Ross, Y. Li, M. N. Banis, Y. Li, M. Liu, O. Voznyy, C. T. Dinh, T. Zhuang, P. Stadler, Y. Cui, X. Du, P. Yang, E. H. Sargent, Sulfur-modulated tin sites enable highly selective electrochemical reduction of CO<sub>2</sub> to formate. *Joule* **1**, 794–805 (2017).
23. X. Lu, D. Y. C. Leung, H. Wang, J. Xuan, A high performance dual electrolyte microfluidic reactor for the utilization of CO<sub>2</sub>. *Appl. Energy* **194**, 549–559 (2017).
24. K. Liu, W. A. Smith, T. Burdyny, Introductory guide to assembling and operating gas diffusion electrodes for electrochemical CO<sub>2</sub> reduction. *ACS Energy Lett.* **4**, 639–643 (2019).
25. D. Higgins, C. Hahn, C. Xiang, T. F. Jaramillo, A. Z. Weber, Gas-diffusion electrodes for carbon dioxide reduction: A new paradigm. *ACS Energy Lett.* **4**, 317–324 (2018).
26. S. Ma, R. Luo, J. I. Gold, A. Z. Yu, B. Kim, P. J. A. Kenis, Carbon nanotube containing Ag catalyst layers for efficient and selective reduction of carbon dioxide. *J. Mater. Chem. A* **4**, 8573–8578 (2016).
27. T. Zheng, K. Jiang, N. Ta, Y. Hu, J. Zeng, J. Liu, H. Wang, Large-scale and highly selective CO<sub>2</sub> electrocatalytic reduction on nickel single-atom catalyst. *Joule* **3**, 265–278 (2019).
28. H. B. Yang, S.-F. Hung, S. Liu, K. Yuan, S. Miao, L. Zhang, X. Huang, H.-Y. Wang, W. Cai, R. Chen, J. Gao, X. Yang, W. Chen, Y. Huang, H. M. Chen, C. M. Li, T. Zhang, B. Liu, Atomically dispersed Ni (I) as the active site for electrochemical CO<sub>2</sub> reduction. *Nat. Energy* **3**, 140–147 (2018).
29. Y. Liu, S. Chen, X. Quan, H. Yu, Efficient electrochemical reduction of carbon dioxide to acetate on nitrogen-doped nanodiamond. *J. Am. Chem. Soc.* **137**, 11631–11636 (2015).
30. J.-J. Lv, M. Jouny, W. Luc, W. Zhu, J.-J. Zhu, F. Jiao, A highly porous copper electrocatalyst for carbon dioxide reduction. *Adv. Mater.* **30**, 1803111 (2018).
31. J. Wu, S. Ma, J. Sun, J. I. Gold, C. S. Tiwary, B. Kim, L. Zhu, N. Chopra, I. N. Odeh, R. Vajtai, A. Z. Yu, R. Luo, J. Lou, G. Ding, P. J. A. Kenis, P. M. Ajayan, A metal-free electrocatalyst for carbon dioxide reduction to multi-carbon hydrocarbons and oxygenates. *Nat. Commun.* **7**, 13869 (2016).
32. K. D. Yang, W. R. Ko, J. H. Lee, S. J. Kim, H. Lee, M. H. Lee, K. T. Nam, Morphology-directed selective production of ethylene or ethane from CO<sub>2</sub> on a Cu mesopore electrode. *Angew. Chem. Int. Ed.* **56**, 796–800 (2017).
33. C.-T. Dinh, T. Burdyny, M. G. Kibria, A. Seifitokaldani, C. M. Gabardo, F. P. G. de Arquer, A. Kiani, J. P. Edwards, P. De Luna, O. S. Bushuyev, C. Zou, R. Quintero-Bermudez, Y. Pang, D. Sinton, E. H. Sargent, CO<sub>2</sub> electroreduction to ethylene via hydroxide-mediated copper catalysis at an abrupt interface. *Science* **360**, 783–787 (2018).
34. C. S. Chen, J. H. Wan, B. S. Yeo, Electrochemical reduction of carbon dioxide to ethane using nanostructured Cu<sub>2</sub>O-derived copper catalyst and palladium (II) chloride. *J. Phys. Chem. C* **119**, 26875–26882 (2015).
35. M. S. Xie, B. Y. Xia, Y. Li, Y. Yan, Y. Yang, Q. Sun, S. H. Chan, A. Fisher, X. Wang, Amino acid modified copper electrodes for the enhanced selective electroreduction of carbon dioxide towards hydrocarbons. *Energy Environ. Sci.* **9**, 1687–1695 (2016).
36. T. T. H. Hoang, S. Verma, S. Ma, T. T. Fister, J. Timoshenko, A. I. Frenkel, P. J. A. Kenis, A. Gewirth, Nanoporous copper–silver alloys by additive-controlled electrodeposition for the selective electroreduction of CO<sub>2</sub> to ethylene and ethanol. *J. Am. Chem. Soc.* **140**, 5791–5797 (2018).
37. H. Mistry, A. S. Varela, C. S. Bonifacio, I. Zegkinoglou, I. Sinev, Y.-W. Choi, K. Kisslinger, E. A. Stach, J. C. Yang, P. Strasser, B. R. Cuenya, Highly selective plasma-activated copper catalysts for carbon dioxide reduction to ethylene. *Nat. Commun.* **7**, 12123 (2016).
38. D. Ren, B. S.-H. Ang, B. S. Yeo, Tuning the selectivity of carbon dioxide electroreduction toward ethanol on oxide-derived Cu<sub>2</sub>Zn catalysts. *ACS Catal.* **6**, 8239–8247 (2016).
39. T. T. H. Hoang, S. Ma, J. I. Gold, P. J. A. Kenis, A. A. Gewirth, Nanoporous copper films by additive-controlled electrodeposition: CO<sub>2</sub> reduction catalysis. *ACS Catal.* **7**, 3313–3321 (2017).
40. Y. Liu, Y. Zhang, K. Cheng, X. Quan, X. Fan, Y. Su, S. Chen, H. Zhao, Y. Zhang, H. Yu, M. R. Hoffmann, Selective electrochemical reduction of carbon dioxide to ethanol on a boron-and nitrogen-Co-doped nanodiamond. *Angew. Chem. Int. Ed.* **56**, 15607–15611 (2017).
41. Y. Zhou, F. Che, M. Liu, C. Zou, Z. Liang, P. De Luna, H. Yuan, J. Li, Z. Wang, H. Xie, H. Li, P. Chen, E. Bladt, R. Quintero-Bermudez, T.-K. Sham, S. Bals, J. Hofkens, D. Sinton, G. Chen, E. H. Sargent, Dopant-induced electron localization drives CO<sub>2</sub> reduction to C<sub>2</sub> hydrocarbons. *Nat. Chem.* **10**, 974–980 (2018).
42. K. Jiang, R. B. Sandberg, A. J. Akey, X. Liu, D. C. Bell, J. K. Nørskov, K. Chan, H. Wang, Metal ion cycling of Cu foil for selective C–C coupling in electrochemical CO<sub>2</sub> reduction. *Nat. Catal.* **1**, 111–119 (2018).
43. T.-T. Zhuang, Z.-Q. Liang, A. Seifitokaldani, Y. Li, P. De Luna, T. Burdyny, F. Che, F. Meng, Y. Min, R. Quintero-Bermudez, C. T. Dinh, Y. Pang, M. Zhong, B. Zhang, J. Li, P.-N. Chen, X.-L. Zheng, H. Liang, W.-N. Ge, B.-J. Ye, D. Sinton, S.-H. Yu, E. H. Sargent, Steering post-C–C coupling selectivity enables high efficiency electroreduction of carbon dioxide to multi-carbon alcohols. *Nat. Catal.* **1**, 421–428 (2018).
44. K. Jiang, S. Siahrostami, T. Zheng, Y. Hu, S. Hwang, E. Stavitski, Y. Peng, J. Dynes, M. Gangisetty, D. Su, K. Attenkofer, H. Wang, Isolated Ni single atoms in graphene nanosheets for high-performance CO<sub>2</sub> reduction. *Energy Environ. Sci.* **11**, 893–903 (2018).
45. B. A. Rosen, A. Salehi-Khojin, M. R. Thorson, W. Zhu, D. T. Whipple, P. J. A. Kenis, R. I. Masel, Ionic liquid-mediated selective conversion of CO<sub>2</sub> to CO at low overpotentials. *Science* **334**, 643–644 (2011).
46. I. Ledezma-Yanez, E. P. Gallent, M. T. M. Koper, F. Calle-Vallejo, Structure-sensitive electroreduction of acetaldehyde to ethanol on copper and its mechanistic implications for CO and CO<sub>2</sub> reduction. *Catal. Today* **262**, 90–94 (2016).
47. Y. Zheng, A. Vasileff, X. Zhou, Y. Jiao, M. Jaroniec, S.-Z. Qiao, Understanding the roadmap for electrochemical reduction of CO<sub>2</sub> to multi-carbon oxygenates and hydrocarbons on copper-based catalysts. *J. Am. Chem. Soc.* **141**, 7646–7659 (2019).
48. D. Ren, N. T. Wong, A. D. Handoko, Y. Huang, B. S. Yeo, Mechanistic insights into the enhanced activity and stability of agglomerated Cu nanocrystals for the electrochemical reduction of carbon dioxide to *n*-propanol. *J. Phys. Chem. Lett.* **7**, 20–24 (2015).
49. Y. Hori, I. Takahashi, O. Koga, N. Hoshi, Electrochemical reduction of carbon dioxide at various series of copper single crystal electrodes. *J. Mol. Catal. A Chem.* **199**, 39–47 (2003).
50. R. M. Arán-Ais, D. Gao, B. R. Cuenya, Structure- and electrolyte-sensitivity in CO<sub>2</sub> electroreduction. *Acc. Chem. Res.* **51**, 2906–2917 (2018).
51. D. Gao, R. M. Arán-Ais, H. S. Jeon, B. R. Cuenya, Rational catalyst and electrolyte design for CO<sub>2</sub> electroreduction towards multicarbon products. *Nat. Catal.* **2**, 198–210 (2019).
52. X. Liu, J. Xiao, H. Peng, X. Hong, K. Chan, J. K. Nørskov, Understanding trends in electrochemical carbon dioxide reduction rates. *Nat. Commun.* **8**, 15438 (2017).
53. K. P. Kuhl, E. R. Cave, D. N. Abram, T. F. Jaramillo, New insights into the electrochemical reduction of carbon dioxide on metallic copper surfaces. *Energy Environ. Sci.* **5**, 7050–7059 (2012).
54. G. O. Larrazábal, A. J. Martín, J. Pérez-Ramírez, Building blocks for high performance in electrocatalytic CO<sub>2</sub> reduction: Materials, optimization strategies, and device engineering. *J. Phys. Chem. Lett.* **8**, 3933–3944 (2017).

55. W. Luo, X. Nie, M. J. Janik, A. Asthagiri, Facet dependence of CO<sub>2</sub> reduction paths on Cu electrodes. *ACS Catal.* **6**, 219–229 (2015).
56. W. Tang, A. A. Peterson, A. S. Varela, Z. P. Jovanov, L. Bech, W. J. Durand, S. Dahl, J. K. Nørskov, I. Chorkendorff, The importance of surface morphology in controlling the selectivity of polycrystalline copper for CO<sub>2</sub> electroreduction. *Phys. Chem. Chem. Phys.* **14**, 76–81 (2012).
57. C. W. Li, M. W. Kanan, CO<sub>2</sub> reduction at low overpotential on Cu electrodes resulting from the reduction of thick Cu<sub>2</sub>O films. *J. Am. Chem. Soc.* **134**, 7231–7234 (2012).
58. A. Loidice, P. Lobaccaro, E. A. Kamali, T. Thao, B. H. Huang, J. W. Ager, R. Buonsanti, Tailoring copper nanocrystals towards C<sub>2</sub> products in electrochemical CO<sub>2</sub> reduction. *Angew. Chem. Int. Ed.* **55**, 5789–5792 (2016).
59. E. L. Clark, C. Hahn, T. F. Jaramillo, A. T. Bell, Electrochemical CO<sub>2</sub> reduction over compressively strained CuAg surface alloys with enhanced multi-carbon oxygenate selectivity. *J. Am. Chem. Soc.* **139**, 15848–15857 (2017).
60. Y. Hori, I. Takahashi, O. Koga, N. Hoshi, Selective formation of C<sub>2</sub> compounds from electrochemical reduction of CO<sub>2</sub> at a series of copper single crystal electrodes. *J. Phys. Chem. B* **106**, 15–17 (2002).
61. P. De Luna, R. Quintero-Bermudez, C.-T. Dinh, M. B. Ross, O. S. Bushuyev, P. Todorović, T. Regier, S. O. Kelley, P. Yang, E. H. Sargent, Catalyst electro-redeposition controls morphology and oxidation state for selective carbon dioxide reduction. *Nat. Catal.* **1**, 103–110 (2018).
62. M. P. McDaniel, A review of the Phillips supported chromium catalyst and its commercial use for ethylene polymerization. *Adv. Catal.* **53**, 123–606 (2010).
63. S. Dai, C. Chen, Direct synthesis of functionalized high-molecular-weight polyethylene by copolymerization of ethylene with polar monomers. *Angew. Chem. Int. Ed.* **55**, 13281–13285 (2016).
64. Z. Sun, T. Ma, H. Tao, Q. Fan, B. Han, Fundamentals and challenges of electrochemical CO<sub>2</sub> reduction using two-dimensional materials. *Chem* **3**, 560–587 (2017).
65. H. S. Jeon, S. Kunze, F. Scholten, B. Roldan Cuenya, Prism-shaped Cu nanocatalysts for electrochemical CO<sub>2</sub> reduction to ethylene. *ACS Catal.* **8**, 531–535 (2017).
66. Q. Li, W. Zhu, J. Fu, H. Zhang, G. Wu, S. Sun, Controlled assembly of Cu nanoparticles on pyridinic-N rich graphene for electrochemical reduction of CO<sub>2</sub> to ethylene. *Nano Energy* **24**, 1–9 (2016).
67. S. Y. Lee, H. Jung, N.-K. Kim, H.-S. Oh, B. K. Min, Y. J. Hwang, Mixed copper states in anodized Cu electrocatalyst for stable and selective ethylene production from CO<sub>2</sub> reduction. *J. Am. Chem. Soc.* **140**, 8681–8689 (2018).
68. M. Ma, K. Djanashvili, W. A. Smith, Controllable hydrocarbon formation from the electrochemical reduction of CO<sub>2</sub> over Cu nanowire arrays. *Angew. Chem. Int. Ed.* **55**, 6680–6684 (2016).
69. J. Huang, M. Mensi, E. Oveisi, V. Mantella, R. Buonsanti, Structural sensitivities in bimetallic catalysts for electrochemical CO<sub>2</sub> reduction revealed by Ag-Cu nanodimers. *J. Am. Chem. Soc.* **141**, 2490–2499 (2019).
70. H. Jung, S. Y. Lee, C. W. Lee, M. K. Cho, D. H. Won, C. Kim, H.-S. Oh, B. K. Min, Y. J. Hwang, Electrochemical fragmentation of Cu<sub>2</sub>O nanoparticles enhancing selective CC coupling from CO<sub>2</sub> reduction reaction. *J. Am. Chem. Soc.* **141**, 4624–4633 (2019).
71. S. Ma, M. Sadakiyo, M. Heima, R. Luo, R. T. Haasch, J. I. Gold, M. Yamauchi, P. J. A. Kenis, Electroreduction of carbon dioxide to hydrocarbons using bimetallic Cu-Pd catalysts with different mixing patterns. *J. Am. Chem. Soc.* **139**, 47–50 (2017).
72. Z. W. Ulissi, M. T. Tang, J. Xiao, X. Liu, D. A. Torelli, M. Karamad, K. Cummins, C. Hahn, N. S. Lewis, T. F. Jaramillo, K. Chan, J. K. Nørskov, Machine-learning methods enable exhaustive searches for active bimetallic facets and reveal active site motifs for CO<sub>2</sub> reduction. *ACS Catal.* **7**, 6600–6608 (2017).
73. A. Vasileff, C. Xu, Y. Jiao, Y. Zheng, S.-Z. Qiao, Surface and interface engineering in copper-based bimetallic materials for selective CO<sub>2</sub> electroreduction. *Chem* **4**, 1809–1831 (2018).
74. W. Zhu, B. M. Tackett, J. G. Chen, F. Jiao, Bimetallic electrocatalysts for CO<sub>2</sub> reduction. *Top. Curr. Chem.* **376**, 41 (2018).
75. T. Zheng, K. Jiang, H. Wang, Recent advances in electrochemical CO<sub>2</sub>-to-CO conversion on heterogeneous catalysts. *Adv. Mater.* **30**, 1802066 (2018).
76. C. Kim, F. Dionigi, V. Beermann, X. Wang, T. Möller, P. Strasser, Alloy nanocatalysts for the electrochemical oxygen reduction (ORR) and the direct electrochemical carbon dioxide reduction reaction (CO<sub>2</sub>RR). *Adv. Mater.* **31**, 1805617 (2018).
77. Z. Chang, S. Huo, W. Zhang, J. Fang, H. Wang, The tunable and highly selective reduction products on Ag@Cu bimetallic catalysts toward CO<sub>2</sub> electrochemical reduction reaction. *J. Phys. Chem. C* **121**, 11368–11379 (2017).
78. M. Andersen, A. J. Medford, J. K. Nørskov, K. Reuter, Scaling-relation-based analysis of bifunctional catalysis: The case for homogeneous bimetallic alloys. *ACS Catal.* **7**, 3960–3967 (2017).
79. D. A. Torelli, S. A. Francis, J. C. Crompton, A. Javier, J. R. Thompson, B. S. Brunschwig, M. P. Soriaga, N. S. Lewis, Nickel-gallium-catalyzed electrochemical reduction of CO<sub>2</sub> to highly reduced products at low overpotentials. *ACS Catal.* **6**, 2100–2104 (2016).
80. H. Xiao, W. A. Goddard, T. Cheng, Y. Y. Liu, Cu metal embedded in oxidized matrix catalyst to promote CO<sub>2</sub> activation and CO dimerization for electrochemical reduction of CO<sub>2</sub>. *Proc. Natl. Acad. Sci. U.S.A.* **114**, 6685–6688 (2017).
81. Z.-Q. Liang, T.-T. Zhuang, A. Seifitokaldani, J. Li, C.-W. Huang, C.-S. Tan, Y. Li, P. De Luna, C. T. Dinh, Y. Hu, Q. Xiao, P.-L. Hsieh, Y. Wang, F. Li, R. Quintero-Bermudez, Y. Zhou, P. Chen, Y. Pang, S.-C. Lo, L.-J. Chen, H. Tan, Z. Xu, S. Zhao, D. Sinton, E. H. Sargent, Copper-on-nitride enhances the stable electrosynthesis of multi-carbon products from CO<sub>2</sub>. *Nat. Commun.* **9**, 3828 (2018).
82. H. Jung, S. Y. Lee, C. W. Lee, M. K. Cho, D. H. Won, C. Kim, H.-S. Oh, B. K. Min, Y. J. Hwang, Electrochemical fragmentation of Cu<sub>2</sub>O nanoparticles enhancing selective C–C coupling from CO<sub>2</sub> reduction reaction. *J. Am. Chem. Soc.* **141**, 4624–4633 (2019).
83. D. Ren, Y. Deng, A. D. Handoko, C. S. Chen, S. Malkhandi, B. S. Yeo, Selective electrochemical reduction of carbon dioxide to ethylene and ethanol on Copper(I) oxide catalysts. *ACS Catal.* **5**, 2814–2821 (2015).
84. L. Fan, Z. Xia, M. Xu, Y. Lu, Z. Li, 1D SnO<sub>2</sub> with wire-in-tube architectures for highly selective electrochemical reduction of CO<sub>2</sub> to C<sub>1</sub> products. *Adv. Funct. Mater.* **28**, 1706289 (2018).
85. C. W. Li, J. Ciston, M. W. Kanan, Electroreduction of carbon monoxide to liquid fuel on oxide-derived nanocrystalline copper. *Nature* **508**, 504–507 (2014).
86. J. H. Montoya, A. A. Peterson, J. K. Nørskov, Insights into CC coupling in CO<sub>2</sub> electroreduction on copper electrodes. *ChemCatChem* **5**, 737–742 (2013).
87. Y. Huang, A. D. Handoko, P. Hirunsit, B. S. Yeo, Electrochemical reduction of CO<sub>2</sub> using copper single-crystal surfaces: Effects of CO\* coverage on the selective formation of ethylene. *ACS Catal.* **7**, 1749–1756 (2017).
88. C. Choi, T. Cheng, M. F. Espinosa, H. Fei, X. Duan, W. A. Goddard III, Y. Huang, A highly active star decahedron Cu nanocatalyst for hydrocarbon production at low overpotentials. *Adv. Mater.* **31**, 1805405 (2019).
89. H. Wang, E. Matios, C. Wang, J. Luo, X. Lu, X. Hu, W. Li, Rapid and scalable synthesis of cuprous halide-derived copper nano-architectures for selective electrochemical reduction of carbon dioxide. *Nano Lett.* **19**, 3925–3932 (2019).
90. N. A. Booth, D. P. Woodruff, O. Schaff, T. Gießel, R. Lindsay, P. Baumgärtel, A. M. Bradshaw, Determination of the local structure of glycine adsorbed on Cu (110). *Surf. Sci.* **397**, 258–269 (1998).
91. D. F. Gao, F. Sohoken, B. R. Cuenya, Improved CO<sub>2</sub> electroreduction performance on plasma-activated Cu catalysts via electrolyte design: Halide effect. *ACS Catal.* **7**, 5112–5120 (2017).
92. A. S. Varela, W. Ju, T. Reier, P. Strasser, Tuning the catalytic activity and selectivity of Cu for CO<sub>2</sub> electroreduction in the presence of halides. *ACS Catal.* **6**, 2136–2144 (2016).
93. Y. Wang, D. Wang, C. J. Dares, S. L. Marquard, M. V. Sheridan, T. J. Meyer, CO<sub>2</sub> reduction to acetate in mixtures of ultrasmall (Cu)<sub>n</sub>(Ag)<sub>m</sub> bimetallic nanoparticles. *Proc. Natl. Acad. Sci. U.S.A.* **115**, 278–283 (2018).
94. F. Jia, X. Yu, L. Zhang, Enhanced selectivity for the electrochemical reduction of CO<sub>2</sub> to alcohols in aqueous solution with nanostructured Cu–Au alloy as catalyst. *J. Power Sources* **252**, 85–89 (2014).
95. S. Lee, G. Park, J. Lee, Importance of Ag-Cu biphasic boundaries for selective electrochemical reduction of CO<sub>2</sub> to ethanol. *ACS Catal.* **7**, 8594–8604 (2017).
96. C. G. Morales-Guio, E. R. Cave, S. A. Nitopi, J. T. Feaster, L. Wang, K. P. Kuhl, A. Jackson, N. C. Johnson, D. N. Abram, T. Hatsukade, C. Hahn, T. F. Jaramillo, Improved CO<sub>2</sub> reduction activity towards C<sub>2</sub> alcohols on a tandem gold on copper electrocatalyst. *Nat. Catal.* **1**, 764–771 (2018).
97. C. Hahn, T. Hatsukade, Y.-G. Kim, A. Vaillonis, J. H. Baricuatro, D. C. Higgins, S. A. Nitopi, M. P. Soriaga, T. F. Jaramillo, Engineering Cu surfaces for the electrocatalytic conversion of CO<sub>2</sub>: Controlling selectivity toward oxygenates and hydrocarbons. *Proc. Natl. Acad. Sci. U.S.A.* **114**, 5918–5923 (2017).
98. D. Kim, C. S. Kley, Y. F. Li, P. D. Yang, Copper nanoparticle ensembles for selective electroreduction of CO<sub>2</sub> to C<sub>2</sub>–C<sub>3</sub> products. *Proc. Natl. Acad. Sci. U.S.A.* **114**, 10560–10565 (2017).
99. M. Rahaman, A. Dutta, A. Zanetti, P. Broekmann, Electrochemical reduction of CO<sub>2</sub> into multicarbon alcohols on activated Cu mesh catalysts: An identical location (IL) study. *ACS Catal.* **7**, 7946–7956 (2017).
100. Y. Song, W. Chen, C. Zhao, S. Li, W. Wei, Y. Sun, Metal-free nitrogen-doped mesoporous carbon for electroreduction of CO<sub>2</sub> to ethanol. *Angew. Chem. Int. Ed.* **56**, 10840–10844 (2017).
101. K. Nakata, T. Ozaki, C. Terashima, A. Fujishima, Y. Einaga, High-yield electrochemical production of formaldehyde from CO<sub>2</sub> and seawater. *Angew. Chem. Int. Ed.* **53**, 871–874 (2014).
102. Y. Liu, Y. Zhang, K. Cheng, X. Quan, X. Fan, Y. Su, S. Chen, H. Zhao, Y. Zhang, H. Yu, M. R. Hoffmann, Selective electrochemical reduction of carbon dioxide to ethanol on a Boron- and Nitrogen-Co-doped nanodiamond. *Angew. Chem. Int. Ed. Eng.* **56**, 15607–15611 (2017).
103. X. Zou, M. Liu, J. Wu, P. M. Ajayan, J. Li, B. Liu, B. I. Yakobson, How nitrogen-doped graphene quantum dots catalyze electroreduction of CO<sub>2</sub> to hydrocarbons and oxygenates. *ACS Catal.* **7**, 6245–6250 (2017).

104. D. M. Weekes, D. A. Salvatore, A. Reyes, A. Huang, C. P. Berlinguette, Electrolytic CO<sub>2</sub> reduction in a flow cell. *Acc. Chem. Res.* **51**, 910–918 (2018).
105. X. Lu, D. Y. C. Leung, H. Wang, M. K. H. Leung, J. Xuan, Electrochemical reduction of carbon dioxide to formic acid. *ChemElectroChem* **1**, 836–849 (2014).
106. Y. Wang, P. Han, X. Lv, L. Zhang, G. Zheng, Defect and interface engineering for aqueous electrocatalytic CO<sub>2</sub> reduction. *Joule* **12**, 2551–2582 (2018).
107. A. D. Handoko, C. W. Ong, Y. Huang, Z. G. Lee, L. Lin, G. B. Panetti, B. S. Yeo, Mechanistic insights into the selective electroreduction of carbon dioxide to ethylene on Cu<sub>2</sub>O-derived copper catalysts. *J. Phys. Chem. C* **120**, 20058–20067 (2016).
108. F.-Y. Zhang, T. Sheng, N. Tian, L. Liu, C. Xiao, B.-A. Lu, B.-B. Xu, Z.-Y. Zhou, S.-G. Sun, Cu overlayers on tetrahedral Pd nanocrystals with high-index facets for CO<sub>2</sub> electroreduction to alcohols. *Chem. Commun.* **53**, 8085–8088 (2017).
109. N. Gutiérrez-Guerra, L. Moreno-López, J. Serrano-Ruiz, J. Valverde, A. de Lucas-Consuegra, Gas phase electrocatalytic conversion of CO<sub>2</sub> to syn-fuels on Cu based catalysts-electrodes. *Appl. Catal. B Environ.* **188**, 272–282 (2016).
110. B. Endrődi, G. Bencsik, F. Darvas, R. Jones, K. Rajeshwar, C. Janáky, Continuous-flow electroreduction of carbon dioxide. *Prog. Energy Combust. Sci.* **62**, 133–154 (2017).
111. Y. C. Li, D. Zhou, Z. Yan, R. H. Gonçalves, D. A. Salvatore, C. P. Berlinguette, T. E. Mallouk, Electrolysis of CO<sub>2</sub> to syngas in bipolar membrane-based electrochemical cells. *ACS Energy Lett.* **1**, 1149–1153 (2016).
112. J. Wu, F. G. Risalvato, P. P. Sharma, P. J. Pellechia, F.-S. Ke, X.-D. Zhou, Electrochemical reduction of carbon dioxide II. Design, assembly, and performance of low temperature full electrochemical cells. *J. Electrochem. Soc.* **160**, F953–F957 (2013).
113. J. Wu, F. G. Risalvato, S. Ma, X.-D. Zhou, Electrochemical reduction of carbon dioxide III. The role of oxide layer thickness on the performance of Sn electrode in a full electrochemical cell. *J. Mater. Chem. A* **2**, 1647–1651 (2014).
114. D. T. Whipple, E. C. Finke, P. J. A. Kenis, Microfluidic reactor for the electrochemical reduction of carbon dioxide. *Solid State Lett.* **13**, B109–B111 (2010).
115. S. Verma, X. Lu, S. Ma, R. I. Masel, P. J. A. Kenis, The effect of electrolyte composition on the electroreduction of CO<sub>2</sub> to CO on Ag based gas diffusion electrodes. *Phys. Chem. Chem. Phys.* **18**, 7075–7084 (2016).
116. S. Ma, Y. Lan, G. M. J. Perez, S. Moniri, P. J. A. Kenis, Silver supported on titania as an active catalyst for electrochemical carbon dioxide reduction. *ChemSusChem* **7**, 866–874 (2014).
117. K. Hara, A. Kudo, T. Sakata, Electrochemical reduction of carbon dioxide under high pressure on various electrodes in an aqueous electrolyte. *J. Electroanal. Chem.* **391**, 141–147 (1995).
118. M. Bevilacqua, J. Filippi, H. A. Miller, F. Vizza, Recent technological progress in CO<sub>2</sub> electroreduction to fuels and energy carriers in aqueous environments. *Energy Technol.* **3**, 197–210 (2015).
119. K. Hara, A. Tsuneto, A. Kudo, T. Sakata, Electrochemical reduction of CO<sub>2</sub> on a Cu electrode under high pressure factors that determine the product selectivity. *J. Electrochem. Soc.* **141**, 2097–2103 (1994).
120. Y. i. Hori, in *Modern Aspects of Electrochemistry* (Springer, 2008), pp. 89–189.
121. D. S. Ripatti, T. R. Veltman, M. W. Kanan, Carbon monoxide gas diffusion electrolysis that produces concentrated C<sub>2</sub> products with high single-pass conversion. *Joule* **3**, 240–256 (2019).
122. T. Burdyny, W. A. Smith, CO<sub>2</sub> reduction on gas-diffusion electrodes and why catalytic performance must be assessed at commercially-relevant conditions. *Energy Environ. Sci.* **12**, 1442–1453 (2019).
123. R. L. Cook, R. C. MacDuff, A. F. Sammells, High rate gas phase CO<sub>2</sub> reduction to ethylene and methane using gas diffusion electrodes. *J. Electrochem. Soc.* **137**, 607–608 (1990).
124. J. Li, G. Chen, Y. Zhu, Z. Liang, A. Pei, C.-L. Wu, H. Wang, H. R. Lee, K. Liu, S. Chu, Y. Cui, Efficient electrocatalytic CO<sub>2</sub> reduction on a three-phase interface. *Nat. Catal.* **1**, 592–600 (2018).
125. O. G. Sánchez, O. G. Sánchez, Y. Y. Birdja, M. Bulut, J. Vaes, T. Breugelmans, D. Pant, Recent advances in industrial CO<sub>2</sub> electroreduction. *Curr. Opin. Green Sustain. Chem.* **16**, 47–56 (2019).
126. T. E. Teeter, P. Van Rysselberghe, Reduction of carbon dioxide on mercury cathodes. *J. Chem. Phys.* **22**, 759–760 (1954).
127. C. Xia, P. Zhu, Q. Jiang, Y. Pan, W. Liang, E. Stavitski, H. N. Alshareef, H. Wang, Continuous production of pure liquid fuel solutions via electrocatalytic CO<sub>2</sub> reduction using solid-electrolyte devices. *Nat. Energy* **4**, 776–785 (2019).
128. S. Zhong, Z. Cao, X. Yang, S. M. Kozlov, K.-W. Huang, V. Tung, L. Cavallo, L.-J. Li, Y. Han, Electrochemical conversion of CO<sub>2</sub> to 2-bromoethanol in a membraneless cell. *ACS Energy Lett.* **4**, 600–605 (2019).
129. A. Paris, A. B. Bocarsly, High-efficiency conversion of CO<sub>2</sub> to oxalate in water is possible using a Cr-Ga oxide electrocatalyst. *ACS Catal.* **9**, 2324–2333 (2019).
130. Y. C. Li, Z. Wang, T. Yuan, D.-H. Nam, M. Luo, J. Wicks, B. Chen, J. Li, F. P. G. de Arquer, Y. Wang, C.-T. Dinh, O. Voznyy, D. Sinton, E. H. Sargent, Binding site diversity promotes CO<sub>2</sub> electroreduction to ethanol. *J. Am. Chem. Soc.* **141**, 8584–8591 (2019).

#### Acknowledgments

**Funding:** This work was supported by the National Key R&D Program of China (2018YFA0209600 and 2016YFA0202900), the National Natural Science Foundation of China (NSFC; grant nos. 21878268 and 21676242), and Rice University. H.W. is a CIFAR Azrieli Global Scholar in the Bio-inspired Solar Energy Program. L.F. acknowledges support from the China Scholarship Council (CSC) (201806320253) and 2018 Zhejiang University Academic Award for Outstanding Doctoral Candidates. C.X. acknowledges support from a J. Evans Attwell-Welch postdoctoral fellowship provided by the Smalley-Curl Institute. **Author contributions:** Y. L. and H.W. supervised the project. L.F. and C.X. wrote the manuscript with the support from all authors and drafted the introduction, electrocatalysts section, and outlook part. F.Y. and J.W. summarized the ECR reactor part. **Competing interests:** The authors declare that they have no competing interests. **Data and materials availability:** All data needed to evaluate the conclusions in the paper are present in the paper. Additional data related to this paper may be requested from the authors.

Submitted 6 June 2019

Accepted 3 December 2019

Published 21 February 2020

10.1126/sciadv.aay3111

**Citation:** L. Fan, C. Xia, F. Yang, J. Wang, H. Wang, Y. Lu, Strategies in catalysts and electrolyzer design for electrochemical CO<sub>2</sub> reduction toward C<sub>2+</sub> products. *Sci. Adv.* **6**, eaay3111 (2020).



## Strategies in catalysts and electrolyzer design for electrochemical CO<sub>2</sub> reduction toward C<sub>2</sub>+ products

Lei Fan, Chuan Xia, Fangqi Yang, Jun Wang, Haotian Wang and Yingying Lu

*Sci Adv* 6 (8), eaay3111.  
DOI: 10.1126/sciadv.aay3111

### ARTICLE TOOLS

<http://advances.sciencemag.org/content/6/8/eaay3111>

### REFERENCES

This article cites 129 articles, 15 of which you can access for free  
<http://advances.sciencemag.org/content/6/8/eaay3111#BIBL>

### PERMISSIONS

<http://www.sciencemag.org/help/reprints-and-permissions>

Use of this article is subject to the [Terms of Service](#)

---

*Science Advances* (ISSN 2375-2548) is published by the American Association for the Advancement of Science, 1200 New York Avenue NW, Washington, DC 20005. The title *Science Advances* is a registered trademark of AAAS.

Copyright © 2020 The Authors, some rights reserved; exclusive licensee American Association for the Advancement of Science. No claim to original U.S. Government Works. Distributed under a Creative Commons Attribution NonCommercial License 4.0 (CC BY-NC).